JOURNAL OF GEOPHYSICAL RESEARCH, VOL. 100, NO. B3, PAGES 4011–4033, MARCH 10, 1995

Active thrust front of the Greater Caucasus: The April 29, 1991, Racha earthquake sequence and its tectonic implications

E. G. Triep,[1] G. A. Abers,[2] and A. L. Lerner-Lam[1]

Lamont-Doherty Earth Observatory of Columbia University, Palisades, New York

V. Mishatkin, N. Zakharchenko, and O. Starovoit

United Methodological Expedition, Institute of the Physics of the Earth, Obninsk, Russia

Abstract. Although fault-bounded thrust sheets are common in the geological record, seismic evidence for their motion is sparse. The April 29, 1991, Racha earthquake (M_S = 7.0), the largest instrumentally recorded earthquake in the Greater Caucasus, is one of the largest recent earthquakes in continental thrust belts and provides evidence on mechanisms of thrust sheet motion. Using data from a deployment of Program for Array Seismic Studies of the Continental Lithosphere (PASSCAL) digital seismographs and various other instruments, we locate 1952 aftershocks occurring between May 7 and June 30, 1991. The aftershocks form a zone ~70 km long and 10-25 km wide striking E-W, following the Racha ridge at the southern boundary of the Greater Caucasus thrust system. Teleseismic body waves are inverted for source parameters of the mainshock and the two largest aftershocks. The solutions show thrust faulting with centroid depths of 3-10 km, comparable to depths of locally recorded aftershocks (~2-12 km). The shallow-dipping nodal plane, the aftershock distribution, and surface geology demonstrate that the main event was caused by faulting on a thrust system dipping NNE at 20°-31° bounding the southern slope of the Greater Caucasus. This fault system thrusts the Greater Caucasus structures south over the Dzhirula basement massif. The inferred fault geometry suggests that the active fault is either a detachment between sediments and Dzhirula basement or cuts through the basement at shallow depths. The 1500-m-high Racha ridge overlies the aftershock zone and is a likely consequence of repeated similar earthquakes. Hence the 1991 earthquake sequence shows that the western Greater Caucasus is accommodating plate convergence at a rate possibly comparable to the eastern Greater Caucasus (a few millimeters per year). Along-strike geological discontinuities above and below the thrust surface correspond to the eastern end of the mainshock rupture area. No strong evidence for transfer structures could be found along strike, suggesting that differences in collisional style between the western and eastern Greater Caucasus may reflect differences in mechanical properties rather than differences in convergence rate. A June 15, 1991, event and its aftershocks, southeast of the primary aftershock zone along strike, show fault planes and slip vectors rotated ~41° clockwise from the mainshock. This rotation is consistent with an along-strike change in direction of the thrust front, near 44°E longitude, and demonstrates strong local structural or topographic control on slip direction. The rotation requires along-strike shortening within the Greater Caucasus thrust system at a rate comparable to the rate of thrusting.

Introduction

Low-angle fault surfaces populate many continental thrust belts in the geological record as a primary mechanism to accommodate convergence. However, in most active thrust belts such surfaces are rarely observed to slip seismically. Several classes of active fault geometry are observed in active collisional belts, including one-sided underthrusting such as the Himalaya [e.g., *Baranowski et al.*, 1984], distributed high-angle faulting of the basement such as the Zagros [e.g., *Jackson and McKenzie*, 1984], and two-sided underthrusting such as the Tien Shan [e.g., *Nelson et al.*, 1987]. In most of these cases the earthquake fault surfaces dip at a moderate to high angle even though subhorizontal faults are apparent from surface geology. A notable exception is the Himalaya, where focal mechanism solutions and gravity and other geophysical data imply a coherent shallow underthrusting (15° to 30°) of India beneath the Lesser Himalaya in accordance with the dips of geologically mapped thrust faults [e.g., *Molnar*, 1984].

One difficulty in understanding the nature of thrusting associated with large continental earthquakes has been the lack of direct, local information on the geometry of their aftershock

[1] Also at Department of Geological Sciences, Columbia University, New York.

[2] Now at Department of Geology, University of Kansas, Lawrence.

Paper number 94JB02597.
0148-0227/95/94JB-02597$05.00

zones. Many compressional belts are remote, making it difficult to deploy local seismic instruments with sufficient density to learn about local faulting processes. Several of the few locally studied continental thrust earthquakes show diffuse aftershocks zones and/or complex fault distribution. Examples include the 1978 Tabas-e-Golshan, Iran, earthquake [*Berberian*, 1982], the 1988 Tennant Creek, Australia, earthquake [*Bowman et al.*, 1990], the 1983 Coalinga, California, earthquake [*Stein and Ekström*, 1992], and the 1985 Kettleman Hills North Dome, California, earthquake [*Ekström et al.*, 1992]. Aftershocks of most of these events do not fall on a single planar fault and indicate that complex fault geometries may typify continental thrust sequences.

The Racha earthquake of April 29, 1991, (M_S = 7.0) and its aftershock sequence took place along the southern slope of the central segment of the Greater Caucasus (Figure 1), a Plio-Quaternary collisional mountain belt [*Zonenshain et al.*, 1990]. In this paper we present results from local network aftershock studies and broadband body wave inversion of the 1991 mainshock and its larger aftershocks. We find that the main fault plane dips toward the highest mountains at a shallow angle (20°-31°), following surface faults that bound thrust sheets, demonstrating that thrust sheet emplacement can occur seismically. In several ways, our results document the importance of structural control on fault segmentation, and show how mechanical heterogeneity of

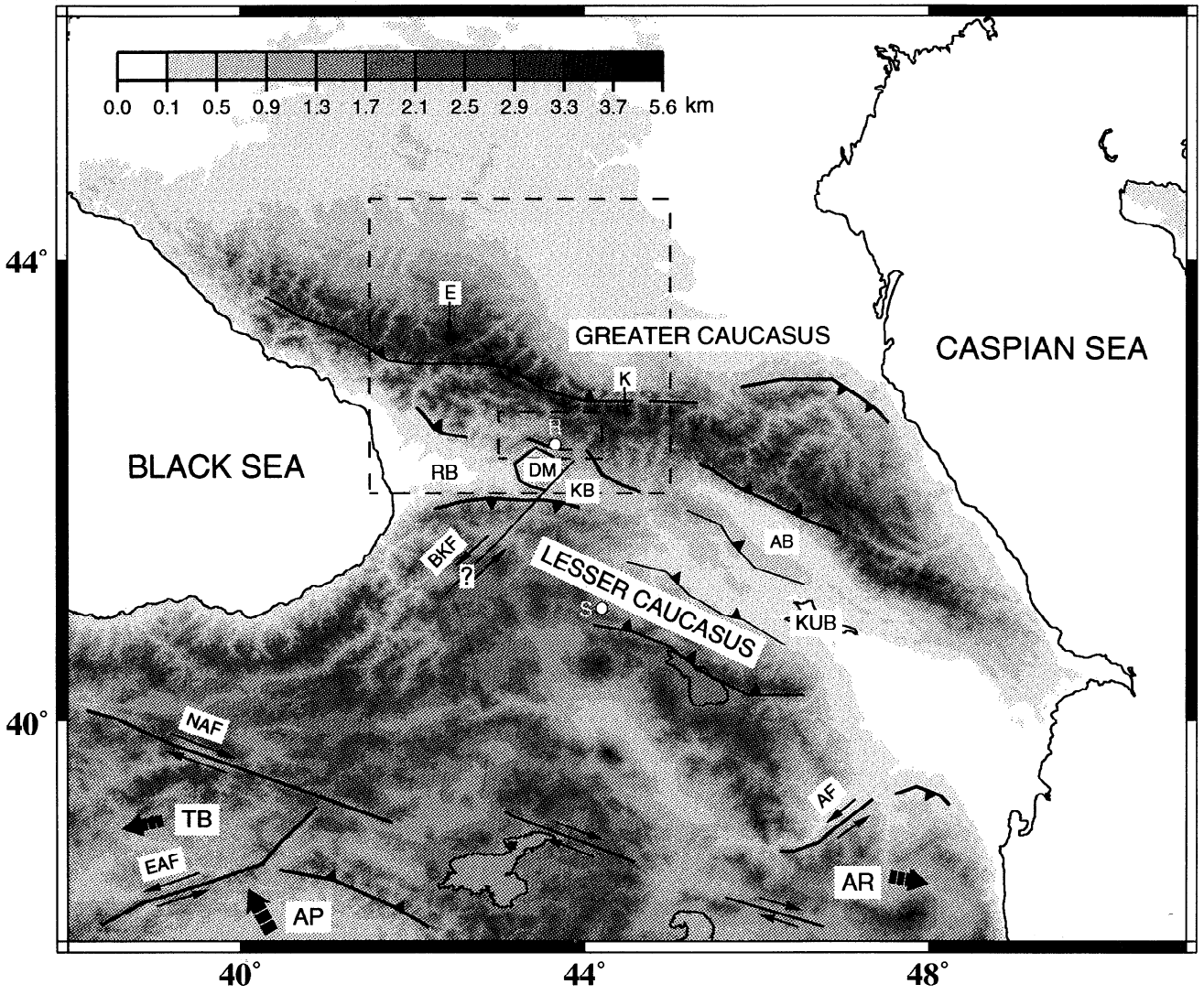

Figure 1. Topographic map of Caucasus Region (contoured at 400-m intervals). Solid lines are faults [*Philip et al.*, 1989; *Jackson*, 1992]. Large dashed arrow shows relative direction of motion of the Arabian plate respect to Eurasia [*DeMets et al.*, 1990]. Shorter dashed arrows show approximate directions of motion for the Turkish and Azerbaijan blocks, and coupled arrows show sense of motion of the strike-slip faults [*Jackson*, 1992]. Circles show epicenters of the 1991 (M_S = 7.0) Racha (R) and 1988 (M_S = 6.8) Spitak (S) earthquakes, the largest instrumentally recorded earthquakes in the Caucasus. Abbreviations are AB, Alazani basin; AF, Araxes River fault zone; AP, Arabian plate; AR, Azerbaijan block; BKF, inferred Borzhomi-Kazbeg fault zone; DM, Dzirula massif; E, Elbruz volcano; EAF, East Anatolian fault zone; K, Kazbeg volcano; KB, Karthaliny basin; KUB, Kura basin; NAF, North Anatolian fault; RB, Rioni basin; and TB, Turkish block. The big dashed rectangle shows the stations deployment area (Figure 3), and the small rectangle inside is the aftershock area. The gray scale topography is shown at the top left.

continental thrust zones may play an important role in rupture processes.

Tectonic Setting

The Eurasian and Arabian plates converge at 29 mm/yr along N26°W near the Caucasus [*De Mets et al.*, 1990]. Subduction of continental crust is avoided by lateral extrusion of the Turkish block, the Azerbaijan block, and the northwestern Iranian block (Figure 1) [*McKenzie*, 1972; *Jackson and McKenzie*, 1984; *Jackson*, 1992] and by crustal thickening through underthrusting of accreted terranes. This region of accreted terranes has been postulated to be an example of "indenter" tectonics [*Philip et al.*, 1989], requiring a left-lateral strike-slip feature bounding the collisional region on the west (the Borzhomi-Kasbeg shear zone, Figure 1). In another model for this region [*Jackson*, 1992], the oblique component of the convergence predicted between Arabia and Eurasia is partitioned into shortening in the north, perpendicular to the strike of the Greater Caucasus, and into right-lateral strike-slip on ESE-WNW striking faults farther south (Figure 1).

The core of the Greater Caucasus consists of Precambrian and Paleozoic igneous and metamorphic rocks related to Paleozoic collisions [*Zonenshain et al.*, 1990; *Khain*, 1979a,b]. The upper Paleozoic rocks in the northern Peredovoy Range have similarities to European rocks [*Zonenshain et al.*, 1990]. The southern slope of the Greater Caucasus is mainly formed of back arc basin sediments, deposited north of a Mesozoic Lesser Caucasus volcanic arc [*Zonenshain and Le Pichon*, 1986; *Zonenshain et al.*, 1990]. Sedimentation was continuous throughout the Jurassic, Cretaceous, and Paleogene. Facies distributions and prior absence of clastics from Greater Caucasus sources show that uplift here began in the middle-late Miocene [*Kopp and Shcherba*, 1985; *Dotduyev*, 1986]. Deformation may have intensified during the middle Pliocene [Burtman, 1989].

Between the Greater and Lesser Caucasus a crystalline basement terrane, the Dzhirula massif, has been trapped in the collision (Figure 1). The massif shows affinities to the Hercynian structures of Europe, unlike Gondwanan microcontinents farther south [*Zonenshain and Le Pichon*, 1986]. Paleomagnetic data from late Paleozoic rocks suggest an intermediate position between Eurasia and Gondwanaland [*Asanidze et al.*, 1980]. A Jurassic-Cretaceous sedimentary sequence lies unconformably above the block and forms its sedimentary cover. The Dzirula Massif is overthrust on its south flank by the Lesser Caucasus [*Burtman*, 1989; *Gamkrelidze*, 1949] and to the north by the Greater Caucasus. The buried part of the Dzirula massif continues to the west into the Black Sea [*Zonenshain and Le Pichon*, 1986]. As discussed below, the 1991 earthquake took place where the Greater Caucasus is overthrusting the Dzirula massif.

Paleomagnetic data indicate a post-Cretaceous N-S convergence of about 900 ± 350 km between the Lesser Caucasus and the Russian platform [*Burtman*, 1989; *Bazhenov and Burtman*, 1987], although the reliability of these numbers has been questioned [*Satian et al.*, 1987]. Folds and overthrusts of the Greater Caucasus account for some shortening, estimated as about 200 km since late Eocene at the earliest [*Dotduyev*, 1986; *Khain*, 1984]. Part of the shortening may have been accommodated since the end of Miocene by a north dipping subduction zone north of the Lesser Caucasus back arc basins [*Zonenshain and Le Pichon*, 1986; *Khalilov et al.*, 1987]. Intermediate depth earthquakes are found in earthquake catalogs for the eastern Caucasus [*Lebedeva*, 1958; *Tskhakaya*, 1962; *Khalilov et al.*, 1987; *Godzikovskaya*, 1988; *Godzikovskaya and Reysner*, 1989], which suggest a subducted slab there, although the depths of these earthquakes are not well constrained. Quaternary volcanism (which may also provide evidence for subduction) exists only in the western Caucasus where there is no evidence of intermediate depth earthquakes (Figure 2).

Thrust sheet structures (nappes) characterize deformation on the southern slope of the Greater Caucasus. Surface geology [*Milanovsky and Khain*, 1963; *Dotduyev*, 1986; *Philip et al.*, 1989] shows thrust sheets transported south, with the Eurasian margin basement thrust over the Mesozoic basin sediments, and these thrust over the adjacent basins and massif still further south (Figure 1). Deeper layers were involved in thrusting later than shallower layers, and the most recent thrusting involved crystalline basement [*Dotduyev*, 1986]. In the youngest zones of deformation, the faults bounding the thrust sheet complexes are subhorizontal where exposed.

Several important differences have been pointed out between the western and eastern Caucasus [*Philip et al.*, 1989], roughly divided along 44°E longitude (Figure 1). (1) The western Greater Caucasus has concentrated deformation at its southern slope, while the northern flank is almost undeformed. In the east, deformation occurs on both flanks. (2) Plio-Quaternary volcanism is present only in the western Greater Caucasus (from Kazbeg to Elbruz, Figure 1). (3) Thrust faults on the northern boundary of the western Lesser Caucasus dip to the south, while in the east section these faults dip to the north (Figure 1). (4) Bouguer gravity anomalies [*Ruppel and McNutt*, 1990] and topography suggest a displacement to the north of the inferred crustal root of the eastern Greater Caucasus relative to the western part. (5) Additionally, we note that exposures of unroofed basement in the Greater Caucasus are present in the west but are absent in the east. *Philip et al.* [1989] used some of these differences to infer the presence of a major left-lateral shear zone separating the western from eastern Caucasus. As discussed below, other explanations are possible.

Seismicity

Historical records [Gorshkov, 1984] suggest that no earthquake with magnitude larger than 7.0 has occurred since 1800 in the Caucasus Region, although there is substantial lower-magnitude seismicity (Figure 2). The December 7, 1988, (M_S = 6.8) Spitak earthquake in Lesser Caucasus (Figures 1 and 2) is the largest recent earthquake prior to the Racha earthquake. Before 1991, an east-west trend of seismicity is seen in the vicinity of the Racha earthquake (42.4°N, 43.6°E). Farther west, seismicity follows the southern slope of the Greater Caucasus. These events are small (magnitude < 5) and their focal mechanisms are unknown, except for one earthquake at 43.1°N, 41.5°E (July 16, 1963; M_S = 6.5, Figure 2) [*Jackson and McKenzie*, 1984]. In the east, seismicity rates are higher than in the western section, and earthquakes occur on both sides of the range. Twelve earthquakes with $m_b > 5$ have reported focal mechanisms (*Jackson and McKenzie* [1984] and Harvard centroid-moment tensor solutions [e.g., *Dziewonski et al.*, 1992a]). Their mechanisms (Figure 2) suggest shallow underthrusting dipping toward the highest mountains on each side [*Jackson and McKenzie*, 1984]. The selection of the nodal plane is not directly constrained, although it is consistent with the Neogene fault geometry. In the western Caucasus the 1991 Racha earthquake [*Zaharova et al.*, 1993] and aftershock sequence (events I, II, III, IV and V; see Figure 2) show thrust faulting. The October 23, 1992, earthquake (M_S = 6.5, event IX; see Figure 2)

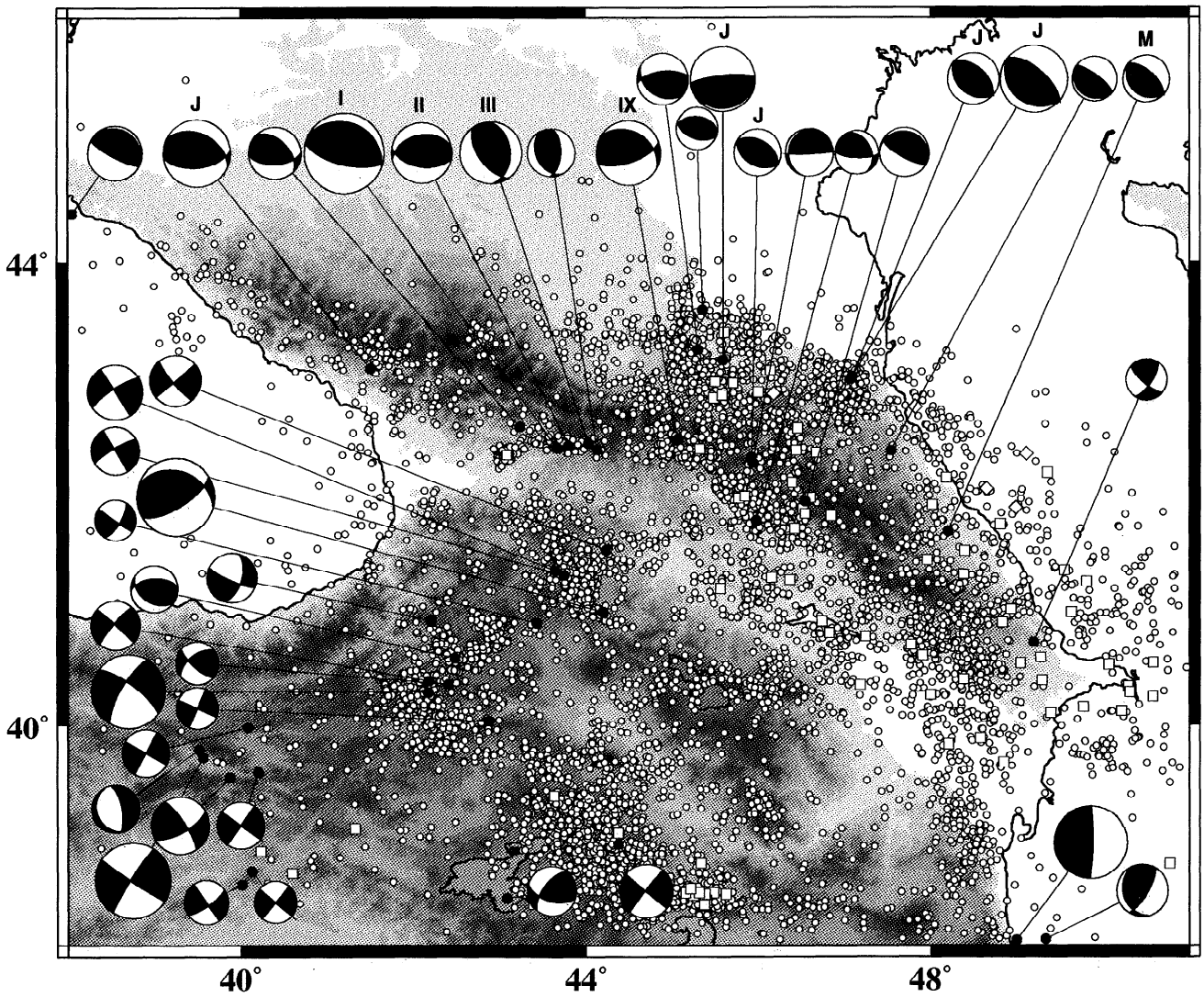

Figure 2. Seismicity 1962-1987 obtained from the Soviet catalog (Soviet Academy of Sciences, Institute of Physics of the Earth, Earthquakes in the USSR, published yearly, by Nauka Publishing House, Moscow). Small open circles and squares are earthquakes with depth $\leq$ 60 km and > 60 km respectively. Larger solid circles show epicenters from the National Earthquake Information Center (NEIC) of earthquakes with focal mechanisms. Locations of the 1991 Racha earthquake (I) and its aftershocks (II, III, and the event west of I and the one east of III) are from this paper (Table 3). I, II, III, and IX (event M_S = 6.7 on October 23, 1992) have mechanisms from this paper (Table 4). The mechanisms labeled J are from *Jackson and McKenzie* [1984]. M is from *McKenzie* [1972]. All other mechanisms are centroid moment tensor (CMT) [e.g., *Dziewonski et al.*, 1992a]. The gray scale topography is same as in Figure 1.

near the boundary between western and eastern Greater Caucasus has a thrust faulting component.

Aftershock Location With Temporary Network

Aftershock data were obtained from two local sources: (1) a Program for Array Seismic Studies of the Continental Lithosphere (PASSCAL)/Joint Seismic Program network with nine portable instruments (Figure 3 and Table 1) operated under the auspices of the Joint Seismic Program of Incorporated Research Institutions for Seismology (IRIS) [*Lerner-Lam et al.*, 1991] and (2) a complementary network of temporary instruments installed by Cambridge University, Institute de Physique du Globe (IPG), Strasbourg, Institute of Physics of the Earth, Moscow, and the U.S. Geological Survey (Figure 3) [*McCormack et al.*, 1992]. The PASSCAL network was operated in the eastern half of the epicentral area, in southern Ossetia, while the Cambridge/IPG network was operated in the western half.

The PASSCAL stations (Table 1 and Figure 3) had three-component sensors of various types, recorded in a triggered mode on Ref-Tek 16-bit data loggers at 100 samples per second and lower sample rates. All stations (except KVA before May 22) were locked to the Omega timing signal, and all were checked against a common clock standard at every data pickup. A clock drift problem at KVA was corrected by frequent external clock checks. Hence all stations have time accuracy better than 0.01 s. Station coordinates were determined with navigation-quality Global Positioning System (GPS) receivers (better than 100 m accuracy).

For PASSCAL data, the P arrival times were measured from the vertical component and most S times from horizontal

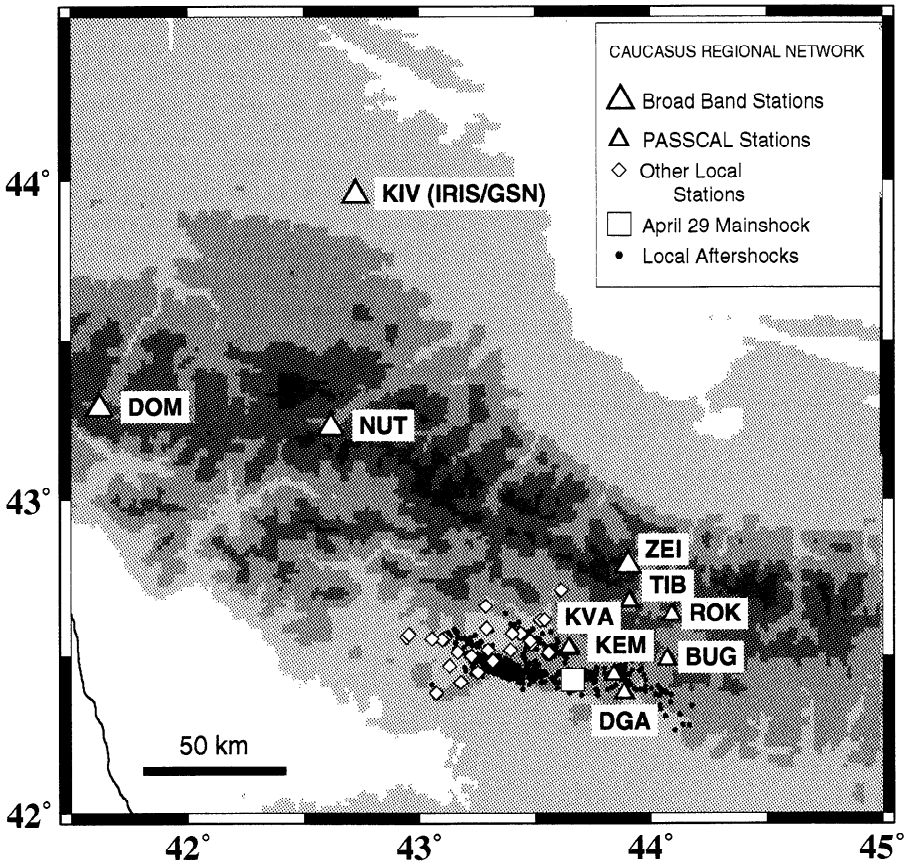

Figure 3. Locations of the Program for Array Seismic Studies of the Continental Lithosphere (PASSCAL) and other temporary stations with best located aftershocks (as described in text) of the 1991 earthquake. Topography is contoured at 1000-m intervals. Line in southwestern corner is Black Sea coast.

components, along with picking uncertainties. Because three-component records were available, we were able to pick *S* arrivals for 99.7% of the seismograms for which we picked *P* arrivals. The *P* and *S* arrival time data from both networks were integrated into one unified set of data for the period May 7 to June 30, 1991. Aftershocks were initially located by the Hypoinverse code [*Klein*, 1978]. We tested by trial and error a suite of velocity models based on ad hoc perturbations to velocity and density structures found in the literature for nearby regions. The best ad hoc model had total variance of arrival time residuals of 0.154 s^2. The velocity model used by the Georgian Academy of Sciences (L. Delitzin, personal communication, 1992; model 1 in Table 2) had a total variance of arrival time residuals 5.1% higher.

Final hypocenters were determined in a joint inversion with velocities by a relocation technique, a one-dimensional version of that used by *Roecker* [1982], *Roecker et al.* [1987], and *Abers and Roecker* [1991]. Velocity was parameterized by one-dimensional

Table 1. Program for Array Seismic Studies of the Continental Lithosphere (PASSCAL) Stations

	Latitude, deg	Longitude, deg	Operation Period	*P* Residual, s	*S* Residual, s
BUG	42.4891	44.0701	May 14, 1991	0.17	0.52
DGA	42.3823	43.8859	May 7 to June 16, 1991	0.18	0.48
DOM	43.2878	41.6190	April 23 to June 30, 1991	4.81	3.14
KEM	42.4414	43.8408	May 15 to June 6, 1991	-0.01	0.57
KVA	42.5225	43.6495	May 11 to May 22, 1991	0.10	0.12
KVA2	42.5275	43.6468	May 22 to June 6, 1991	-0.29	0.00
NUT	43.2260	42.6177	April 30 to June 30, 1991	0.28	-0.07
TIB	42.6742	43.9094	May 13 to May 22, 1991	0.06	0.06
ROK	42.6305	44.0915	May 3 to May 22, 1991	0.03	0.15
ZEI	42.7877	43.9010	April 20, 1991, to March 6, 1992	0.14	0.25

Table 2a. Velocity Model 1

P Velocity, km/s	Depth Range, km
4.5	0 - 2
5.70	2 - 24
6.43	24 - 45
7.9	45 - ∞

Table 2b. Velocity Model 2

P Velocity, km/s	*S* Velocity, km/s	Depth Range, km
4.83	2.61	-3 - 3
5.44	3.19	3 - 7
5.98	3.51	7 - 19
6.33	3.65	19 - 44
8.10*	4.68*	44 - ∞

*Velocity not solved by inversion.

horizontally layered model, and *P* and *S* arrival times were inverted for both *P* and *S* velocities and hypocenters. The best fitting ad hoc velocity model was used as starting model. We inverted the arrivals in the following steps. From the 805 aftershocks recorded at eight or more stations with at least 10 picked phases, a subset of 435 aftershocks was selected using a grading scheme of location quality [*Roecker et al.*, 1987] with the following constraints: (1) hypocenter condition numbers (the ratio of largest to smallest eigenvalues in the hypocentral inversion) less than 80, (2) less than 1 km change in hypocenter for the final iteration, and (3) root-mean-square residual of the arrival times less than 0.5 s. These 435 events were inverted jointly for velocity and hypocenters. Station corrections (Table 1) were calculated as a separate step from the weighted average residual at a given station. The travel times were corrected, and the iterative procedure was started again. The variance changes after the first iteration were negligible. Velocities in the mantle half space were unresolved. With the final model (model 2, Table 2) and corrections, all 1952 aftershocks were relocated (Figures 4a, 4b, and 4d).

To assess the aftershocks location uncertainties, we compared results with a fully nonlinear location technique [*Roecker et al.*,

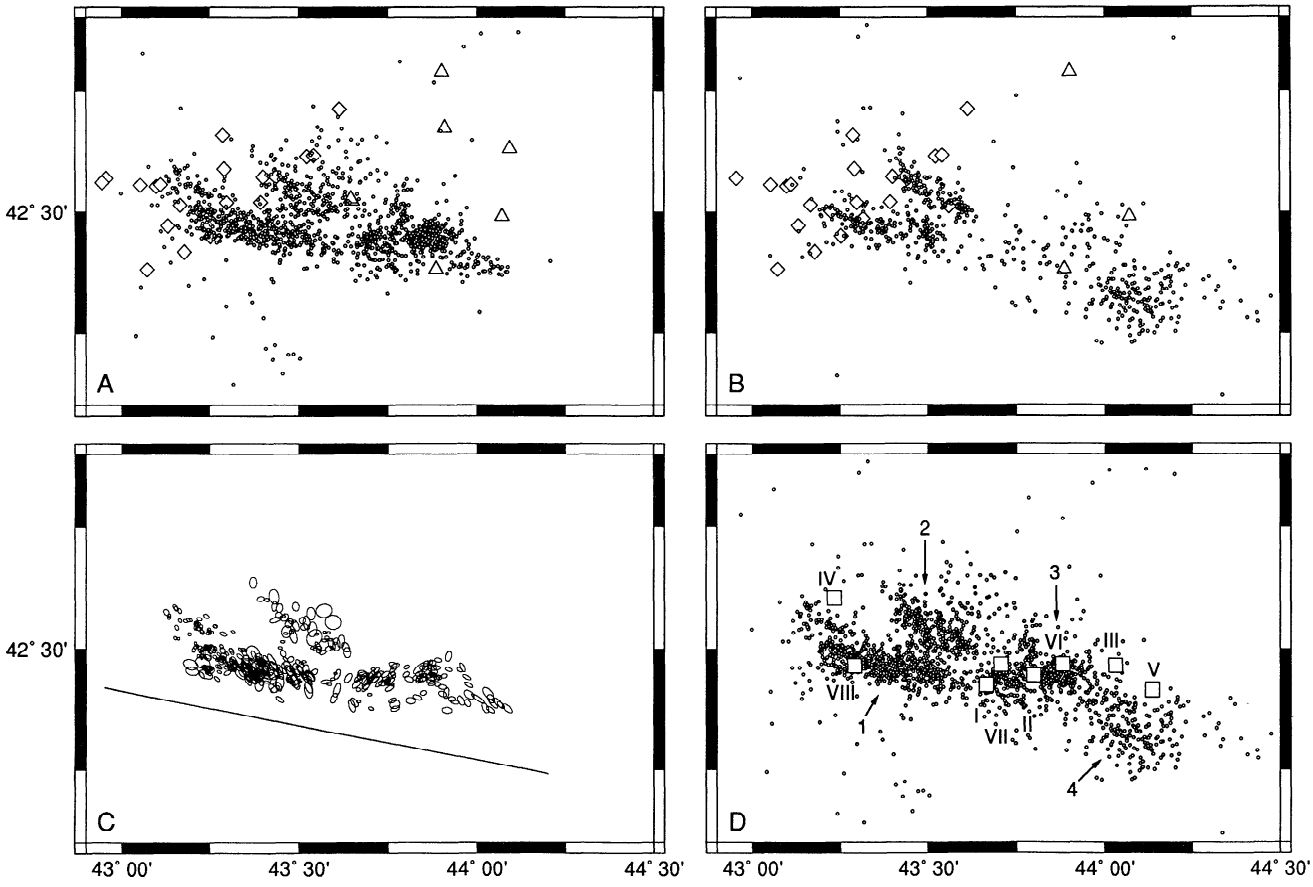

Figure 4. Aftershock locations, determined from temporary station records, occurring between May 7 and June 30: all located events (a) before and (b) after the June 15 earthquake (event III). Triangles show Program for Array Seismic Studies of the Continental Lithosphere (PASSCAL) stations operating in the corresponding periods. Diamonds show other local stations. (c) 2.4σ ellipses of epicentral locations for the 410 best located events occurring before event III (errors in latitude, longitude, and depth are no more than 2 km). The line is the intersection of the surface with the regression plane obtained by a least squares procedure (explained in the text) applied to these events. (d) All locally recorded aftershocks and teleseismic relocations of $M_S > 5.0$ events (squares). Teleseismic relocations (Table 3) are relative to the aftershock epicenters obtained from the local networks as described in text. Aftershock clusters are indicated by arrows and are labeled 1, 2, 3, and 4.

1988], which utilizes the formalism of *Tarantola and Valette* [1982]. The technique takes into account a priori uncertainties in the arrival time picks and in the travel times, and it calculates the a posteriori probability density function for a grid of values of the hypocenter coordinates. The marginal probability functions in epicenter were contoured about the regions where the integrated probabilities are 68% and 95%, and hence they defined the corresponding levels of confidence for the epicentral location. The marginal probability function in depth was also estimated.

We performed the calculations for eight aftershocks and compared the results with the formal errors obtained in the linearized inversion. The well located events typically have 68% confidence limits for the largest and smallest horizontal uncertainties about ±1.0 km and ±0.6 km, respectively. The corresponding 95% confidence limits are ±1.7 km and ±0.9 km. The 68% confidence uncertainty limits in depth for these events are on average about ±1.1 km. Poorly located events may typically have 68% confidence limit uncertainties of about ±5 km. We found that these uncertainties are underestimated by the formal errors obtained from the linearized relocations. Although there is a tendency for large uncertainties to be underestimated more than the small ones, we uniformly scale the formal errors by multiplying them by an average factor of 2.4 so that the 68% confidence limits found in nonlinear relocations match 1σ formal errors found in linearized inversion. The resulting errors (e.g., Figures 4c and 13) seem to be appropriate considering other sources of uncertainties (velocity model, picking errors, definition of formal errors, etc.).

Altogether, 717 events were recorded at five or more stations with at least 10 picked phases. A subset of 494 of these events have hypocenter errors (2.4σ) less than or equal to 2 km (Figures 3, 5b, 5c, 12, 13c, and 15) and will be referred to as the best located events in the discussion below. From these 494 events, a subset of 410 (Figure 4c) were recorded before the aftershock on June 15 (event III, Table 3 and Figures 2 and 4d).

Teleseismic Relocation of Large Events

The main shock and several large aftershocks were relocated teleseismically relative to the epicenters obtained from the local network (Figure 4d and Table 3). Four events were located both by the aftershock network and by teleseismic stations and were used to calibrate teleseismic paths from the Caucasus. These events were fixed at the local network hypocenters, and their averaged teleseismic residuals were used as station corrections for locating eight other $M > 5.0$ events in the region (Table 3). A teleseismic version of the fully nonlinear relocation technique was again used [*Abers et al.*, 1993]. Here, the technique takes into account a priori uncertainties in teleseismic picks and theoretical travel times as well as the spatial variation in arrival time residuals, in a calculation of the probability density functions for earthquake epicenters. Predicted times are calculated from the iasp91 travel time tables [*Kennett and Engdahl*, 1991] and from the empirical station corrections. A priori uncertainties and other parameters are selected as by *Abers et al.* [1993]. Uncertainties in the epicenters are obtained using a three-dimensional grid and then integrating over depth. The depth is constrained to be less than 15 km, consistent with the range of aftershock depths. The relocations show that the mainshock (I) is located in the approximate center of the overall aftershock zone near the gap between the western and eastern clusters (Figures 4d and 13c). The June 15 event (III) is west of the primary aftershock area before this event (Figure 4), and other large events are distributed throughout the aftershock zone (Figure 4d).

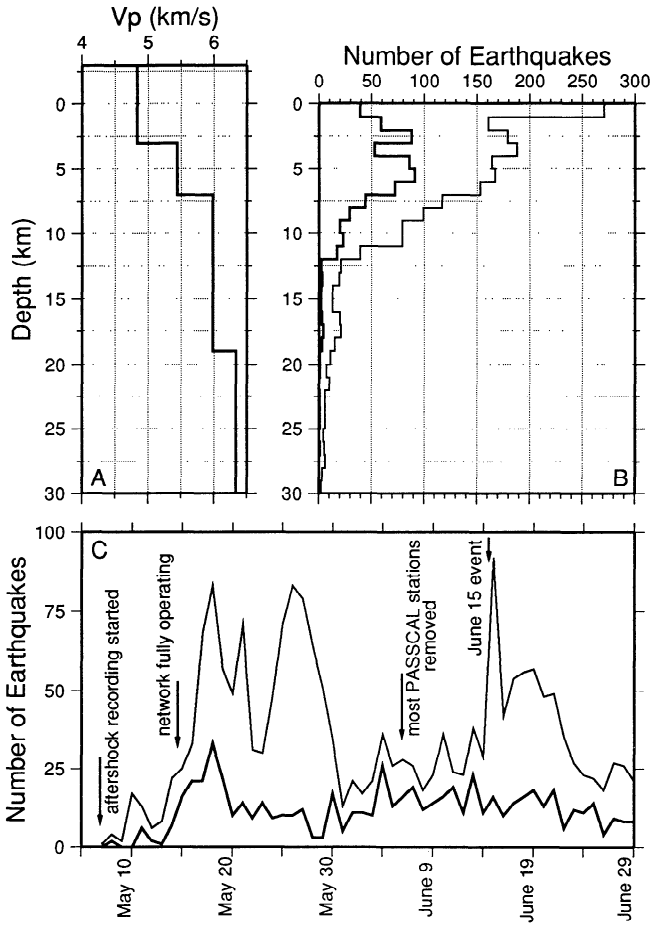

Figure 5. (a) One-dimensional *P* wave velocity obtained in the inversion (model 2, Table 3). (b) Depth distribution for aftershocks recorded by Program for Array Seismic Studies of the Continental Lithosphere (PASSCAL) and other local stations, May 7 to June 30. (c) Number of aftershocks in each day. Light line shows all events (Figures 4a and 4b). Heavy line shows best aftershock locations (494 events), as described in text (also see Figures 12 and 15).

Aftershock Locations

Four groups or clusters of aftershocks are recognized (1, 2, 3 and 4, Figure 4d). The easternmost cluster (east of 44°E) are mostly aftershocks of the June 15 event (Figures 4b and 4d). Some activity is seen in this region before June 15 (Figures 4a and 4c), but the orientation of confidence ellipses (Figure 4c) in the same direction may suggest a mislocation problem. Locations of the aftershocks of the June 15 event are not well constrained since most PASSCAL stations were not operating at that time, but they are generally located southeast of the primary aftershock distribution (Figures 4b and 4d). The other three clusters are better constrained. Two in the west (1 and 2, Figures 4c and 4d) trend in W-NW direction, one north of the Racha ridge and one south of it (Figure 15). A third group in the east (3, Figures 4c and 4d), trending in a W-SW direction, represents the eastern part of the main aftershock zone. The gap in the west between the northern and southern cluster (1 and 2, Figures 4c and 4d) and the gap between western and eastern clusters near 43.55°E are well defined judging from the confidence ellipses (Figure 4c).

Only 10 out of the 494 well-located events (Figures 5b, and 13a-13c) are deeper than 12 km, and none are deeper than 18 km.

Table 3. Relocated Epicenters for the Mainshock and Larger Aftershocks

Event	Date	Origin Time, (UT)	m_b	Latitude, deg	Longitude, deg
I	April 29, 1991	0912:48.1	6.2	42.4238 ± .0511	43.6643 ± .0247
II	April 29, 1991	1830:41.5	5.9	42.4434 ± .0432	43.7968 ± .0243
III	June 15, 1991	0059:20.3	6.1	42.4648 ± .0485	44.0297 ± .0260
IV	May 3, 1991	2019:38.8	5.1	42.6025 ± .0491	43.2319 ± .0262
V	July 4, 1991	0626:31.8	5.0	42.4139 ± .0505	44.1348 ± .0280
VI	April 29, 1991	1443:06.4	5.4	42.4671 ± .0467	43.8803 ± .0253
VII	April 29, 1991	1823:15.3	5.5	42.4659 ± .0443	43.7054 ± .0343
VIII	April 29, 1991	2032:54.2	5.4	42.4635 ± .0401	43.2895 ± .0254
IX*	Oct. 23, 1992	2319:47.2	6.7	42.50	45.000

Origin times and magnitudes are from National Earthquake Information Center (NEIC).
* Location is from NEIC.

Clustering at 3 km may be an artificial clumping around the boundary of the velocity model (Figures 5a and 5b and Table 2), but the maximum around 5 km depth for the subset of well-located events is well constrained. Seismicity in the western cross section of best located events (Figure 13a) dips to the north. The range of the aftershocks depths in the eastern section (Figure 13b, cluster 3 in Figure 4d) is comparable to the southwestern cluster. This aftershock distribution is similar in overall dimension to that obtained from permanent network data [*Zaharova et al.*, 1993].

Teleseismic Body Wave Inversion

Data and Procedures

We determine source parameters for events I, II, III, and IX (Table 3) by inverting broadband *P* and *SH* waveforms for these events recorded by global digital networks and the Palisades, New York station (PAL). When broadband seismograms are not directly available (stations SLR, SCP, and LON), corresponding short- and long-period seismograms are combined into one broadband record [*Harvey and Choy*, 1982]. All records are deconvolved to displacement except for some long-period data (labeled "GD" in figures 8a, 8b, 9a, 9b, and 11). The broadband displacement seismograms were band-pass filtered using causal three-pole Butterworth filters with cutoffs at frequencies depending on the instrument type and peculiarities of the waveform, with a passband from 0.005-0.02 Hz to 0.5-2.0 Hz. To avoid rays bottoming in the upper mantle and core, the stations are limited to the epicentral range of 30° to 90° for *P* waves and 30° to 70° for *SH* waves.

Earthquake source parameters are estimated by fitting observed with calculated seismograms using the methodology of *Nábělek* [1984, 1985]. The source is parameterized by a double couple mechanism, depth, scalar seismic moment, and far-field time function. The source time function is parameterized as a series of overlapping triangles [*Nábělek*, 1985; *Ekström*, 1987] each 1-2 s long. The source pulse is convolved with geometrical spreading, anelastic attenuation (t* = 0.7 s for *P* waves, 4.0 s for *S* waves), instrumental response, and source structure Green's functions. Observed short-period *P* arrival times are used to constrain the start time of the *P* waves. The crustal structure at the receivers is taken to be a half-space with *P* and *S* wave velocities and density of 6.0 km/s, 3.46 km/s, and 2750 kg/m^3, respectively. The crustal structure at the source is assumed to be velocity model 2 (Table 2). The results of the inversions and 1σ formal errors are summarized in Table 4 and Figures 6-10.

Mainshock Results

The inversion gives an unexpectedly shallow centroid depth (4.4 km) for an earthquake with no reported surface rupture. Because our parameters differ significantly for those reported in the CMT catalog, and in order to get more reliable error estimates, several tests were performed. In these tests, the parameter of interest was held fixed while all other parameters were determined by inversion (Figures 7 and 10).

First we tested sensitivity to depth by holding depth fixed to each of a series of values and calculating residual variances. A variance minimum (Figure 10) exists near 4-7 km depth, but the normalized variance is not much different between 3 and 10 km depth. The geographical distribution of the teleseismic stations is asymmetrical, as all stations but SLR and SUR are in the northern hemisphere. The first half-cycle of the *P* wave at SLR and SUR is small but clearly compressional (Figure 6). The same *P* waveform (not shown) is observed at NAI (a World-Wide Standard Seismograph Network (WWSSN) station with shorter epicentral distance than SLR but at nearly the same azimuth). The *P* wave pulse is shortly followed by the large downward spike of the *pP* depth phase. Hence *P* is near nodal, while *pP* is not. This is consistent with a ~70° dip of the southern nodal plane and a shallow northern dipping plane. However, because relative amplitudes are small, the constraints on the depth and dip of the nodal planes imposed by *P* and reflected phases at the southern stations are not properly taken into account by the least squares inversion. Figure 7a shows the observed and synthetic *P* wave fit for solutions at different fixed depths for COL (a representative northern station) and for SLR. The solution at 4.4 km has a poor fit for SLR and improves with depth but not beyond 10 km. For COL the fit becomes poor with increasing depth, and it is unacceptable at depths greater than 10 km. For *SH* waves (Figure 7b) at HIA and KMI (examples of stations to the east), the fits are not acceptable at depths greater than 10 km. We conclude that the centroid depth must lie somewhere between 3 and 10 km. These empirically determined bounds are larger than the computed standard errors (Table 4) but more fairly represent the individual phase constraints.

Table 4. Results of Body Wave Inversions

Event	Strike, deg	Dip, deg	Slip, deg	Depth, km	Moment, N m
I*	292.9±6.2	24.2±2.9	97.7±7.4	4.43±2.1	$(2.25\pm0.09)\times10^{19}$
I†	288	39	106	22	$(3.3)\times10^{19}$
II*	258.5±14.2	39.9±3.5	73.2±9.9	5.27±2.8	$(1.13\pm0.11)\times10^{18}$
II†	261.0	41	104	15	$(1.6)\times10^{18}$
III*	357.5±19.5	37.0±4.6	116.7±10.9	5.84±2.1	$(1.42\pm0.16)\times10^{18}$
III†	16	58	130	15	$(2.9)\times10^{18}$
IV†	315	47	127	15	$(3.1)\times10^{17}$
V†	4	57	108	19.7±2.9	$(1.6)\times10^{17}$
IX*	299.0±8.1	33.1±4.2	132.7±5.7	14.42±1.5	$(2.17\pm0.40)\times10^{18}$
IX†	302	13	144	33	$(3.6)\times10^{18}$

* Results from this paper.
† Centroid moment tensor solutions [*Dziewonski et al.*, 1992a,b].

An increase in dip of the north dipping nodal plane (Figure 7c) would improve the fit of the compressional first pulse of SLR and SUR, but the *SH* wave fits deteriorate progressively and are poor beyond 31°. A dip < 20° would give a nodal or dilatational polarity at SRL and SUR. Hence our best estimate of the bounds for the northern dipping plane are 20° and 31°. The fits of the calculated and observed waveforms are not very dependent on the strike of the shallow dipping plane. However, the strike of the conjugate plane is well constrained. A range of 278°-307° for the strike of the shallow dipping plane is estimated by eye from tests similar to those in Figure 7. We conclude that the mainshock is a dip-slip shallow thrust event with a shallow plane dipping to the north.

We did not obtain a good match at all stations. The synthetic seismograms for *P* waves at SLR and SUR have smaller amplitudes than the observed waves in the first 15 s, while at LON and CCM the opposite occurs. Some solutions (for a particular choice of focal parameters) have better fit *P* waves at the southern stations but have poorer fits for some *SH* waves. The problem of uniqueness may be related to the assumption of point source approximation which may be violated for this large earthquake. Another possibility is that structural complexities in the source region are distorting waveforms, for example, from topographic features and/or dipping layers [*Wiens*, 1989; *Richards et al.*, 1991]. These complexities are not unexpected since the source region is an active thrust front with elevated topography. As will be shown below, similar types of misfits are found for the two large aftershocks (with seismic moments about 16 and 20 times smaller than the mainshock). The smaller of these events has mechanism and depth similar to the mainshock, and the other has similar depth but different mechanism. Because problems are similar for a range of event sizes, we suspect that near-source crustal heterogeneities are significantly affecting the waveforms.

April 29 and June 15 Aftershocks (Events II and III)

The two largest aftershocks are thrust events (Figures 8a and 9a). The mechanism of the April 29 aftershock is similar to the main shock although the north dipping plane has a west-southwest strike direction and a higher dip angle (Figures 6 and 8a). The southern nodal plane dip is consistent with the *P* wave at SLR being less nodal than the mainshock. The solution (Table 4 and Figure 8) does not match the *SH* waves in the eastern stations well. Decreasing the dip of the northern dipping plane progressively improves this match (but not for dips < 32°, Figure 8b), and the solution approaches the mainshock solution. The fit to the *P* wave at SLR and the *SH* wave at the western stations degrades at shallow dips, however. A solution identical to the mainshock (Figure 8b) is not acceptable, because it shows a very small amplitude in the *P* and *SH* synthetic waves at SLR and rather large amplitudes for most of the synthetic *SH* waves. From various tests (Figure 10), the observed and calculated wave forms match for ranges of strike, dip, and depth of 244°-280°, 32°-47°, and 4-10 km, respectively. These ranges and the ones from the mainshock do not exclude the possibility of the two earthquakes having the same mechanisms. Nevertheless, the different characteristics mentioned above suggest that the April 29 aftershock is not an exact replica of the mainshock.

The mechanism of the June 15 aftershock is demonstrably different. There is a clear difference between waveforms of the June 15 and the April 29 aftershocks at some of the stations (Figures 8a and 9a); compare *P* waves for SCP, TOL, and SRL and *SH* waves for TOL, SLR, HIA, LZH, and KMI. Excluding the large mismatch of the *P* wave at GDH we obtained a good fit for all *P* waves and a rather poor fit for the *SH* waves in most of the eastern stations. These mismatches resemble those for the mainshock and April 29 aftershock. From various tests (Figure 10), the ranges of strike, dip, and depth with adequate fits are 339°-18°, 32°-47°, and 4-9 km, respectively. We conclude that the June 15 aftershock represents slip on a different plane than the mainshock.

October 23, 1992 Earthquake (Event IX)

This earthquake is located approximately 100 km east of the eastern end of the aftershock zone of the 1991 Racha earthquake, along the southern thrust front of the Greater Caucasus (Figure 2). The mechanism shows reverse faulting (event IX, Table 4 and Figure 11). The north dipping nodal plane is similar to the corresponding plane of the Racha earthquake but with a steeper dip and it shows significant strike-slip component. The centroid

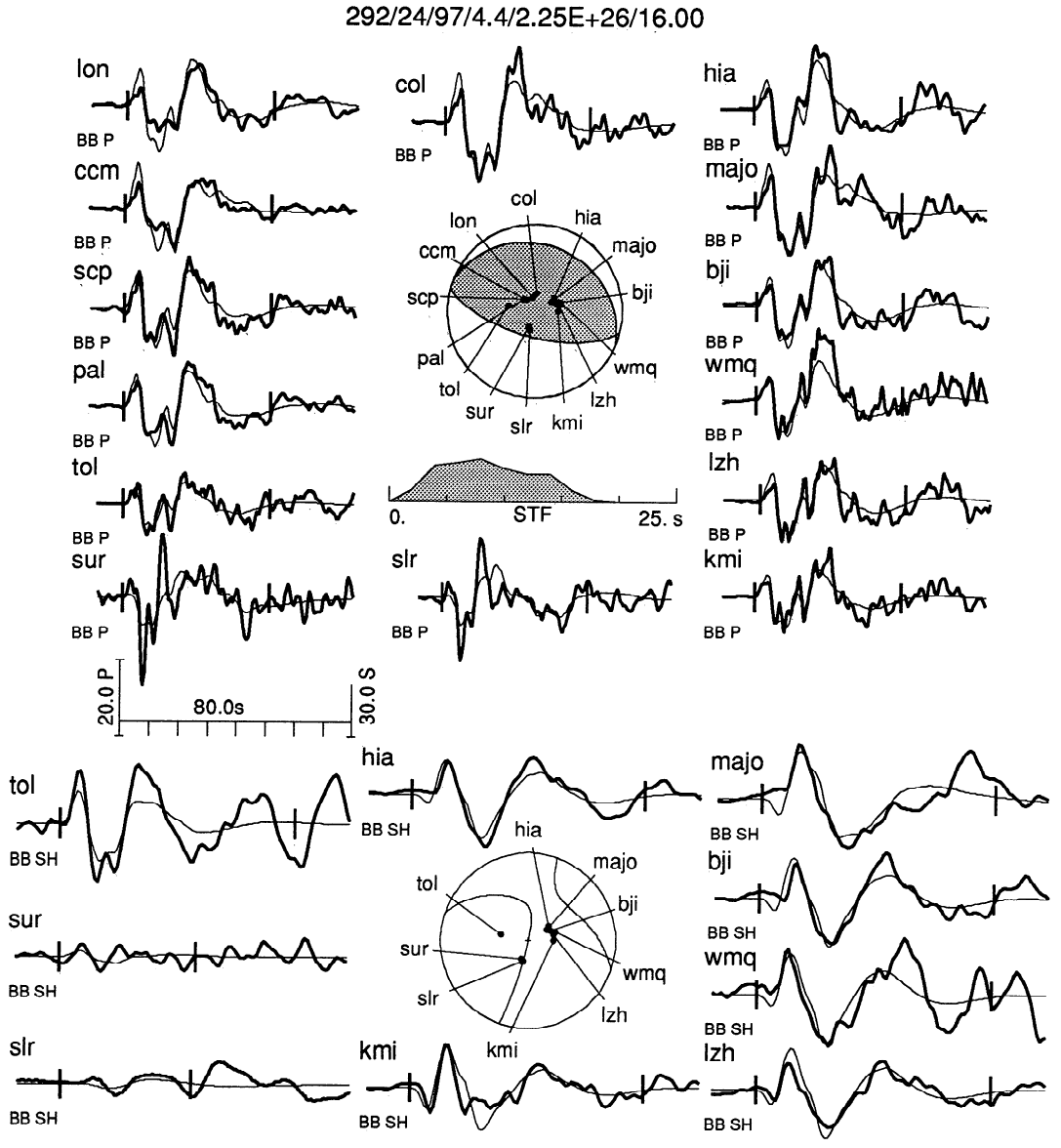

Figure 6. Broadband waveform inversion of Racha mainshock for (top) *P* waves, and (bottom) *SH* waves, with radiation patterns and station distributions. Shaded quadrants denote compressional *P* wave motion. Heavy lines are observed seismograms, and light lines are synthetic waveforms. Waveforms labeled "BB" are broadband. The portions of the seismograms used in the inversion are indicated by vertical lines. Far-field source time function and the time and amplitude scales for seismograms are also shown. Seismogram amplitudes are corrected for geometrical spreading and gain and are normalized independently for each phase (*P* or *SH*). Note different timescales for seismograms and source time function.

depth of 14.4 km is significantly larger than those of the Racha earthquakes.

Comparison of the Body Wave Inversion Results in This Study With the CMT Solutions

Several significant differences are found between our results and the commonly used centroid moment tensor (CMT) catalog (Table 4). The previously discussed tests constrain the depth and dips (e.g., Figures 7a-7c and 10) and together with the aftershock distribution indicate that the CMT depths and dips for these events may not be adequate. For event I a solution with the CMT double-couple source and free depth and moment has a poorer fit to *SH* waveforms than a solution with just the dip fixed to the CMT value of 39° (Figure 7c, bottom) and has 54% of CMT's moment. For event III the CMT solution is somewhat different from our preferred solution but also shows rotation of the nodal planes with respect to the mainshock. Several tests (Figure 9b) compare our solution to the CMT's. Solutions with the mechanism fixed to be identical to the CMT shows a poor fit for the *P* and *SH* waves (particularly for *P* wave at SLR; not shown in Figure 9b). Similar results are obtained in the other tests. Hence we consider the CMT depths and mechanisms for events I and III less reliable than our solutions.

The discrepancies in seismic moment between our solutions and the CMT solutions (Table 4) are harder to explain. For event I, we repeated the above tests with the velocity model PREM

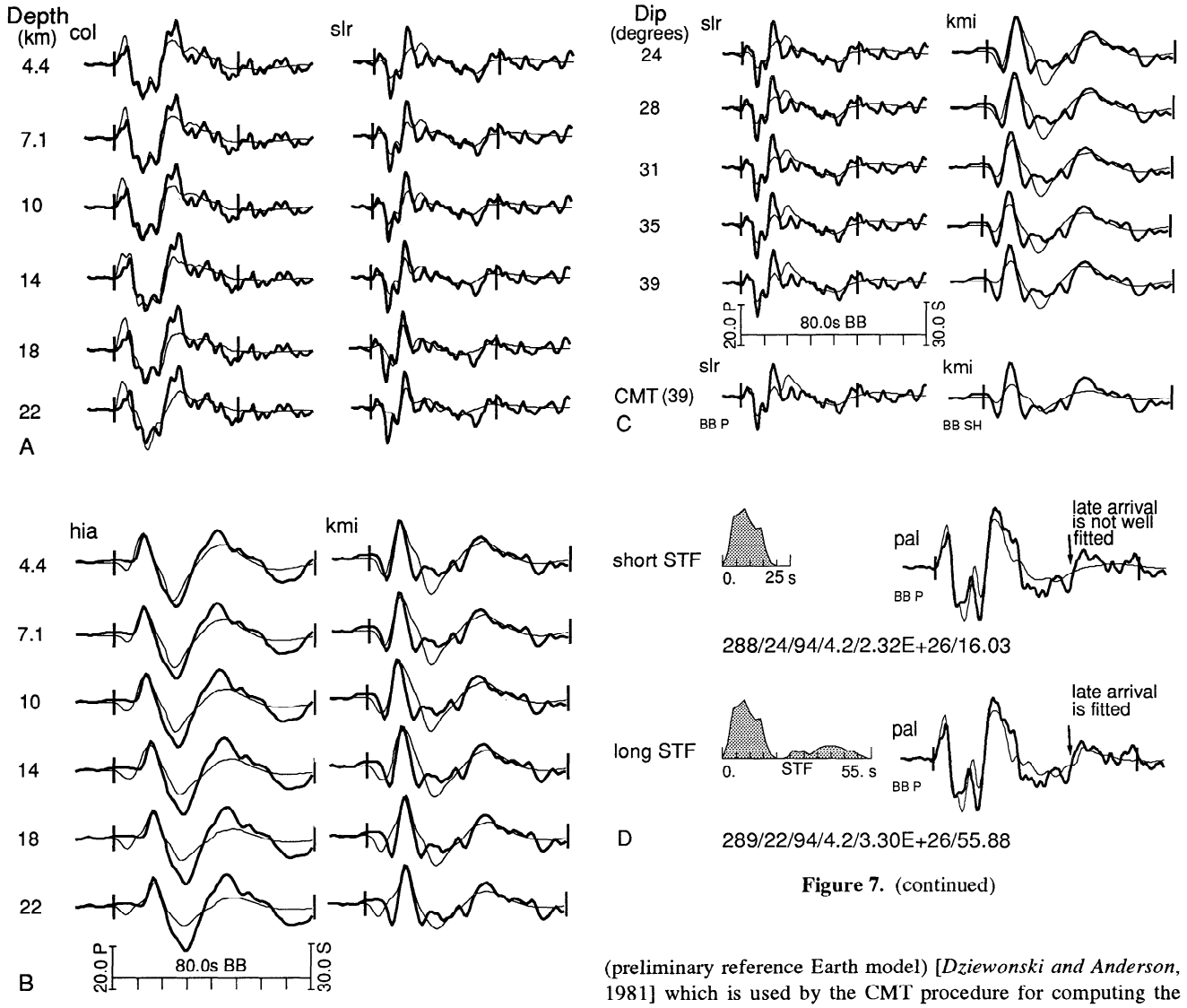

Figure 7. (continued)

Figure 7. (a) Observed (heavy lines) and synthetic (light lines) *P* wave fits for solutions at different fixed depths for stations COL and SLR for the mainshock in each line. The time and amplitude scales are shown at the bottom of Figure 7b. (b) Observed and synthetic *SH* wave fits for solutions at different fixed depths for stations HIA and KMI for the mainshock in each line; depth is fixed as shown, and all other parameters are determined. (c) Observed and synthetic *SH* wave fits for solutions at different fixed dips for stations SLR and KMI for the mainshock in each line; the dip is fixed as shown, and all other parameters are determined. The bottom line shows the solution with strike, dip, and rake fixed to be same as the CMT solution. All waveforms in Figure 6 are solved for, but only the mentioned stations are shown. The time and amplitude scales are also shown. (d) Observed and synthetic seismogram of the *P* waves at station PAL. At the top the source time funtion is same as the used for solution in Table 4, but the inversion windows (segment between vertical lines) are larger. At the bottom, a long source time function is used. The timescale for the seismograms is the same as the source time function. The late arrival is observed in the *P* waves at most of the stations (Figure 6) and is better fitted by the solution with long source time function. The focal parameters of the corresponding solutions are also shown.

(preliminary reference Earth model) [*Dziewonski and Anderson*, 1981] which is used by the CMT procedure for computing the excitation terms (G. Ekström, personal communication, 1994). Since we calculate moment by measuring far-field displacements and by using ray theory, there is a proportionality constant which depends on the velocities and densities assumed at the source and receiver [*Aki and Richards*, 1980, equations 4.88-4.90]. In each of these tests with PREM we obtained a solution with a moment lower than our preferred solution. Hence the excitation differences cannot explain the moment differences.

Likewise, the inverse correlation between moment and depth for shallow events [e.g., *Stein and Wiens*, 1986] cannot account for the moment discrepancies (Table 4). The source is already very shallow, and the centroid would have to be at the surface to give the CMT moment in this way (Figure 10a).

We tested longer source time functions (Figure 7d) than those used in our inversions (Figures 6, 9a, and 11) to investigate possible late release of moment. The resolution of very long period moment release is a frequently suggested problem for body wave inversions [e.g., *Zhang and Lay*, 1989; *Wiens*, 1989]. For event I, we repeated the experiments with a source time function 52 s long and wider inversion windows. The solution with all parameters obtained by inversion is very similar to the solution with the short source time function and same inversion windows (Figure 7d) and has a slight improvement normalized variance misfit (3.3% smaller). The seismic moment is exactly the same as the CMT. The long source time function has an additional

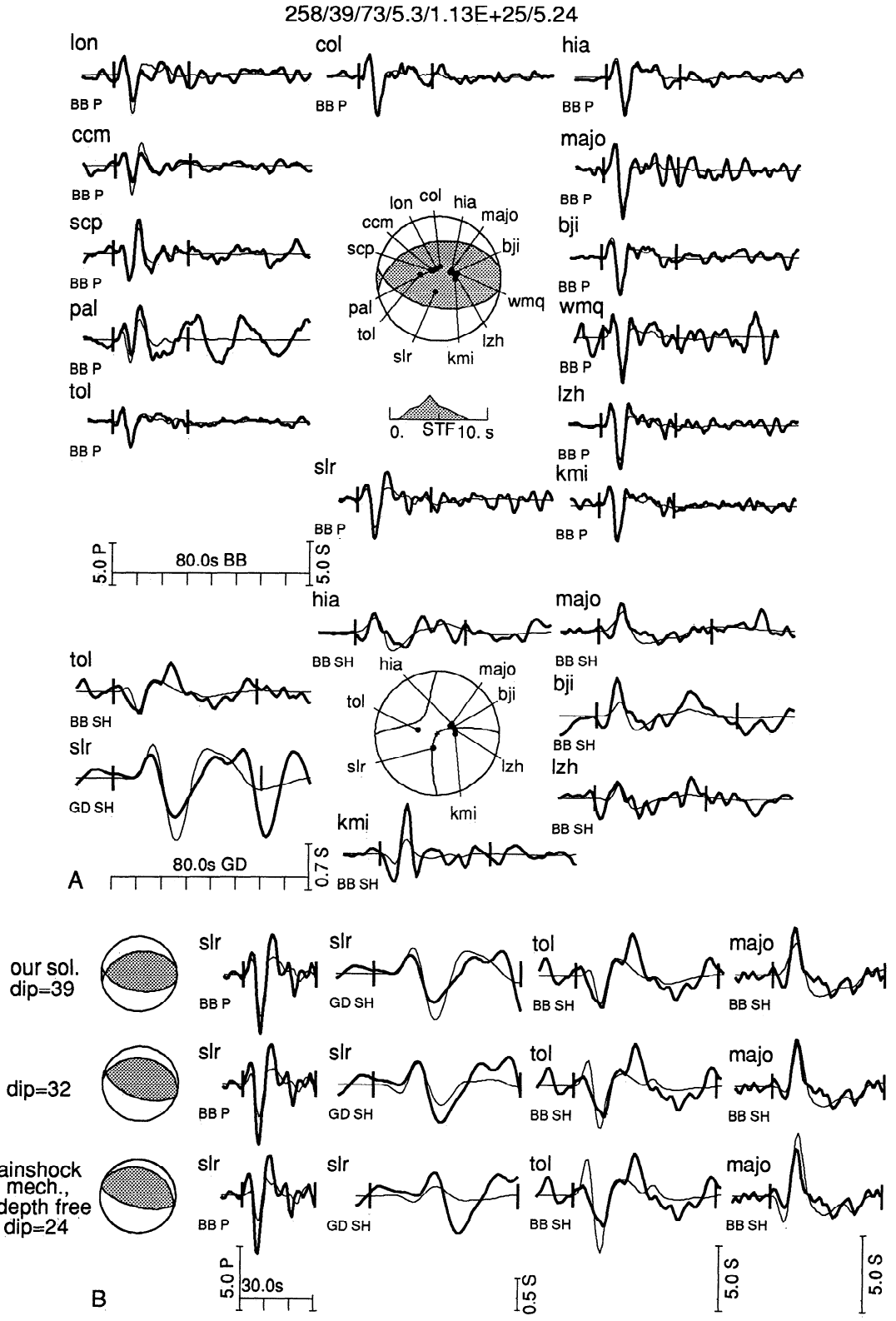

Figure 8. (a) Waveform inversion of the April 29 aftershock. The layout is same as in Figure 6. Waveforms labeled "GD" are Global Digital Seismograph Network (GDSN) long-period traces and are normalized separately; all others labeled "BB" are broadband. (b) Test for shallower dips of the northern dipping plane. Observed (heavy lines) and synthetic (light lines) *P* wave fits at station SLR and *SH* wave fits at stations SLR, TOL, and MAJO for the April 29 aftershock. All waveforms in Figure 8a are solved for, but only the mentioned stations are shown. The following solutions are shown: (1) preferred solution (Table 4), (2) a solution with the dip fixed at 32° allowing the other parameters to be free, and (3) strike, dip, and rake same as the mainshock mechanism (Table 4) with depth and seismic moment free. The corresponding mechanisms are shown to the left and the timescale in the bottom. A solution with a dip of 32° still possible (see text for the discussion). The fit with the preferred mainshock's solution is not acceptable.

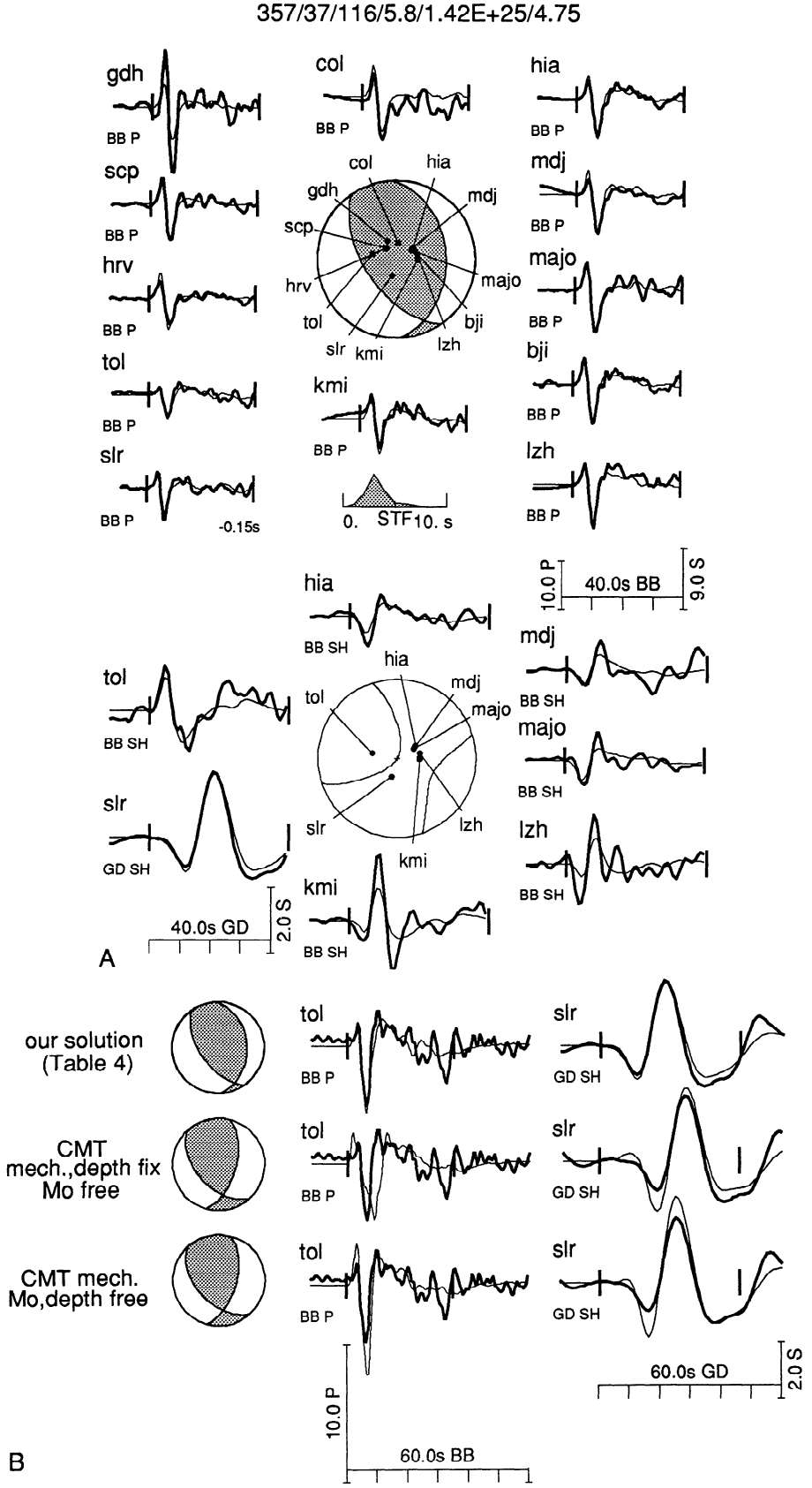

Figure 9. (a) Waveform inversion of the June 15 aftershock. The layout is same as in Figures 6 and 8. (b) Tests to compare the consistency of the preferred solution of the event III (Table 4) against the focal parameters of the centroid moment tensor (CMT) solution for the same earthquake. All waveforms in Figure 9a are solved for, but only *P* wave at station TOL and the *SH* wave of station SLR are shown: (1) solution in Table 4, (2) strike, dip, rake, and depth fixed same as CMT solution with seismic moment free, and (3) strike, dip, and rake fixed same as CMT solution; with depth and seismic moment allowed to be free. The corresponding mechanisms are shown to the left and the timescale at the bottom. Note different amplitude scales for *P* and *S* waves.

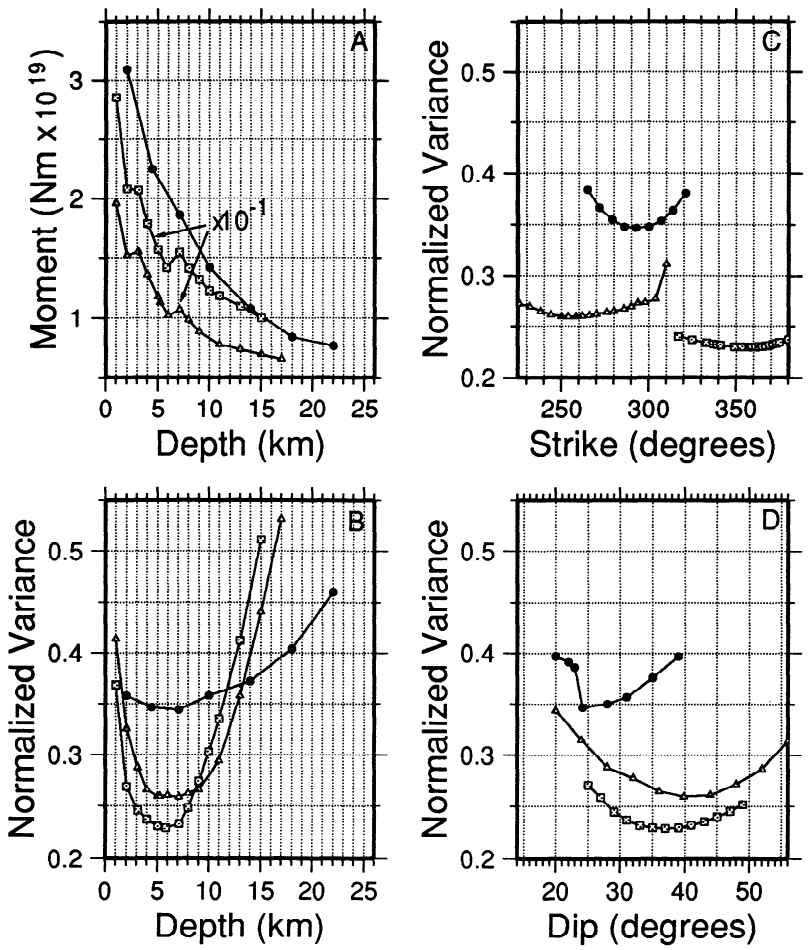

Figure 10. Variation of the seismic moment with (a) depth; and variance reduction with (b) depth, (c) strike, and (d) dip for the main shock (solid circles), April 29 (open triangles), and June 15 (open squares) aftershocks. Variance of residuals is normalized to power in observed seismograms, hence it is unitless. Note that the moment scales for the April 29 and June 15 aftershocks are enlarged 10 times as indicated.

component of moment release between 24 and 52 s (Figure 7d). This result, a late and slow arrival, could explain the moment discrepancy since there may be a lack of bandwidth in our inversion necessary to resolve the total source duration and moment release [e.g., *Ekström*, 1987]. The comparison of the wave form fit obtained with a 20 and 52 s long source time function (Figure 7d) shows that a late arrival at about 60 s is better fit with the longer function. Other earthquakes in active thrust belts with a shallow dipping nodal plane in their source geometry have been found to have long source time process (M_S = 7.3 El Asnam earthquake [*Nábělek*, 1985], M_W = 6.1 Kettleman Hills earthquake [*Ekström et al.*, 1992]). In the El Asnam earthquake the source time function with a second episode of moment release between 20 and 55 s is similar to the long source time function we obtain (Figure 7d). Hence the observed seismograms (and also the tectonic setting) allow the possibility of a late moment release. However, the effect in our case is small and not strictly required by the data, since other effects could be responsible for this apparently late episode (dipping layers, variable bounce-point structure, etc.). Clearly, more work should be done to assess the existence of a late moment release for the Racha earthquake.

For event III we tried a 36-s-long source time function and wider inversion windows looking for a possible long source time process. The source parameters obtained in this case are very similar to those obtained previously, but the moment is still only 76% of the CMT. The additional moment mainly comes from a late moment release between 20 and 35 s, where our excitation models again may be suspect. The U.S. Geological Survey moment tensor solution for this earthquake (Preliminary determination of epicenters (PDE) bulletin) gives a moment similar to the one we obtained with short source time function (Figure 9a and Table 4).

For the event IX a 36-s-long source time function gives a solution very similar to the previous one (Table 4). The moment is 93% of the CMT, but the contribution to the moment release between 10 and 36 s comes from several small and discontinuous peaks in the source time function, whose significance cannot be demonstrated in our present analysis.

Hence after several tests we prefer our solutions to the CMT, but we did not find a clear explanation for the discrepancy in moments. For the mainshock, a late second episode of moment release is allowed by the data but not required. These differences in moment are not central to the issues in this paper, however, and our interpretations should be unaffected by a possible moment bias.

Discussion

Fault Processes at an Active Thrust Front

The aftershocks are north and northeast of the outcrop of the Dzirula massif, and most of their epicenters are within the eastern end of the Gagra-Dzhava zone (GDZ, Figure 12). This zone is a

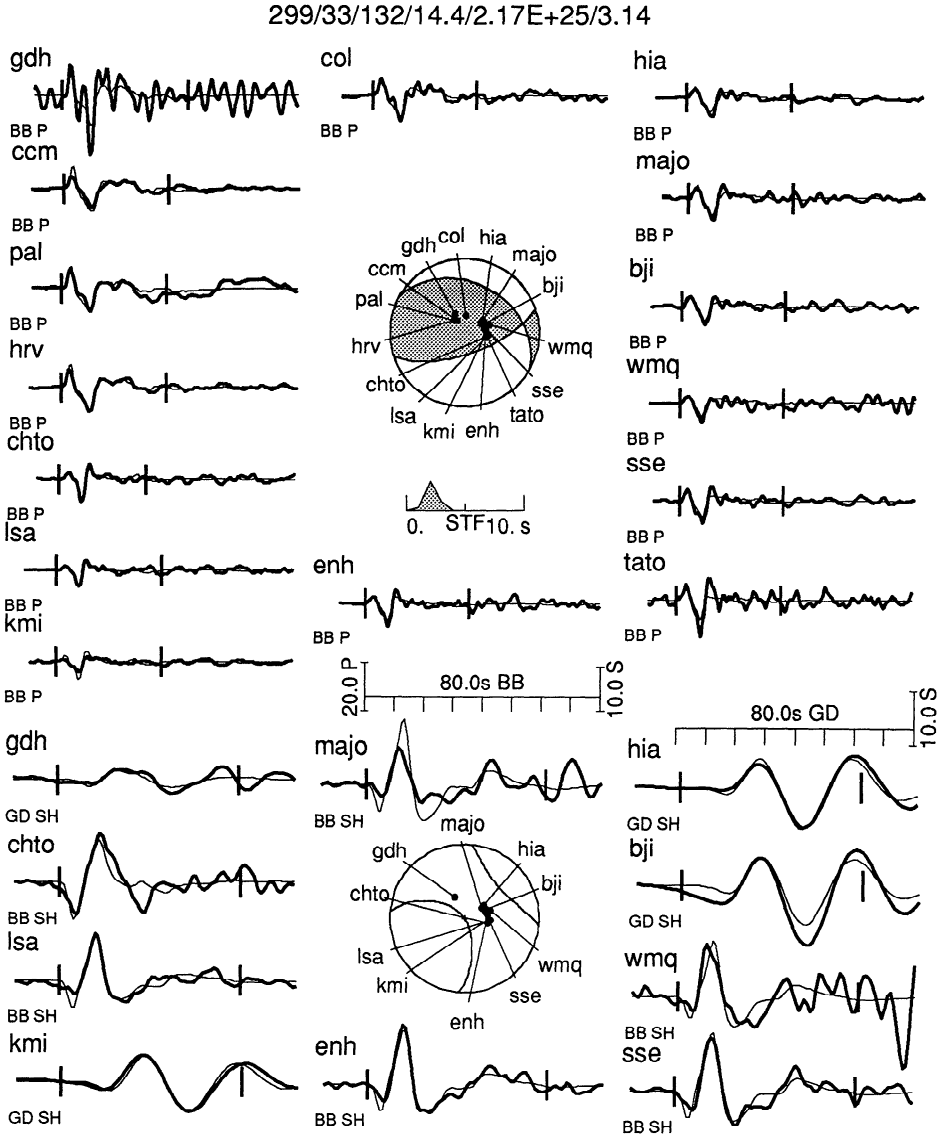

Figure 11. Waveform inversion of the October 23, 1992, earthquake (IX in Tables 3 and 4 and Figure 2). The layout is same as in Figures 6 and 8.

thrust sheet of sedimentary rocks similar to those covering the Dzirula massif. The aftershocks (Figures 3, 12, and 15) are at the southern slope of the Greater Caucasus and are subparallel to the axis of the range, to the strike of the thrust sheets, and to the strike of the nodal planes of the main shock. Surface geology shows that these thrust sheet complexes move on north dipping planes [*Dotduyev*, 1986; *Khain*, 1984], consistent with the shallow-dipping fault plane. The depth distribution (Figure 13a) of the aftershocks is also consistent with the north dipping nodal plane. Hence the north dipping nodal plane is the preferred fault plane.

The preferred nodal plane projects to the surface south of the trace of the Abkhaz-Lechkum fault (Figure 13a), near the fault that bounds the Dzirula massif to the north (Figure 12). Hence this fault zone may have produced the main shock. However, since there is no reported surface rupture for the 1991 Racha earthquake, the rupture may have not reached the surface, and the association with a particular geological fault is tenuous. The absence of surface rupture is hard to verify, however, because political problems made it impossible to adequately survey the potential surface rupture region.

The fault producing the 1991 earthquakes lies at the front of the Greater Caucasus thrust fault system. Either the active fault is a thrust surface separating the Gagra-Dzhava thrust sheet complex from the Dzirula Massif, or the fault lies completely in basement rock, beneath both the Gagra-Dzhava zone and a sliver of the Dzirula massif basement (Figure 14). In other words, either the fault decouples low-strength sediments from high-strength basement rocks (Figure 14a), or the basement is directly involved (Figure 14b). Either interpretation is consistent with the earthquake and its aftershocks being shallow, between 3 and 12 km deep. Large continental earthquakes are often confined to deeper, basement-involved portions of thrust belts [e.g., *Abers et al.*, 1988; *Molnar and Chen*, 1983; *Suárez et al.*, 1983], although some examples exist of large events in sediments (e.g., the Coalinga earthquake [*Stein and Ekström*, 1992]).

Faults, Seismicity Pattern, and Topography

The epicenter distribution has an arcuate shape and follows the E-W striking mapped faults at the surface (Figures 12 and 15). The two southern clusters (1 and 3 in Figures 4d and 15) follow the southern slope of the high Racha ridge [*Nalivkin*, 1976], while

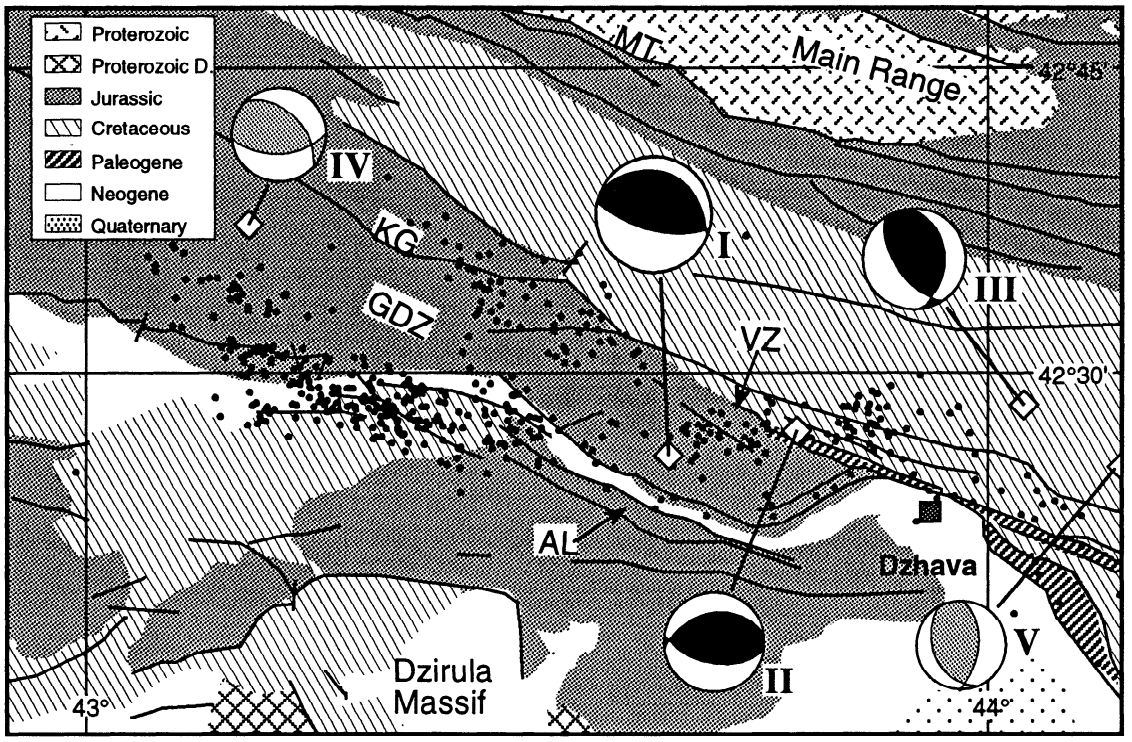

Figure 12. Simplified geologic map [after *Nalivkin*, 1976], with aftershock epicenters and focal mechanisms for the mainshock (I) and four larger aftershocks (II-V; Table 3). The mechanisms for events I, II, and III are from this paper. Events IV and V are Harvard centroid moment tensor (CMT) solutions [*Dziewonski et al.*, 1992a,b]. Solid dots are best aftershock locations (494 events) as described in text. Abbreviations are AL, Abkhaz-Lechkum fault; KG, Krasnuopolyansk-Guzduchay overthrust; MT, Main overthrust; VZ, Vorontsovo-Zanga overthrust; and GDZ, Gagra-Dzhava zone. Proterozoic D distinguishes the basement of the Dzirula massif from the one in the Main Range.

the northwestern cluster is in the Rioni valley north of the ridge. This geometry suggests that the ridge may have been formed by repeated earthquakes similar to the 1991 events. The western part of the ridge bends southwest west of 43.3°E, but the epicenters cross this bend following the mapped faults (Figure 12). In cross section (Figure 13a), the aftershock zone shows a vertical width of some 8 km. If 95% confidence limit errors are allowed, there is a possibility that the aftershock distribution in depth is actually narrower and related to a single fault plane.

The arcuate shape of the epicenter distribution (Figures 4, 12, and 15) suggests that aftershocks may be fitted by a geometrical surface with some curvature. We performed a least squares regression to find the best fitting plane (Figure 4c) and second-degree polynomial surface to the subset of the selected aftershocks that occurred before event III. The F test gives only a 66% probability that the second-degree surface would fit the data better than the plane. The best fitting plane has a strike of 280.8° $\pm$ 1.1° (Figure 4c) and a dip of 17.7° $\pm$ 1.4°, which are consistent with the body wave inversion solution for the main shock. The variations of hypocenters from the regression plane do not show a geometrical pattern that could be easily associated to a secondary surface or different fault. However, diffuse aftershock zones with a diffuse and complex volumetric distribution typify some continental thrust sequences [e.g., *Ekström et al.*, 1992]. This may result from the geometric incompatibility of thrust faulting that requires severe straining in adjacent volumes of rock [*Scholz*, 1990].

If the two western clusters of aftershocks (1 and 2 in Figure 4d) represent slip on two different parts of the same north dipping fault zone, then a gap is present in the seismicity beneath the Racha ridge on the fault (Figures 15 and 13a). Possible explanations for the gap include the following. (1) The mainshock zone of highest slip is in the center of the aftershock zone, and the aftershocks have occurred around the edges of the mainshock zone, where slip gradients (and hence induced shear stresses) are highest (e.g., the 1984 Morgan Hill, California, strike-slip earthquake [*Bakun et al.*, 1986] and the 1971 San Fernando, California, thrust earthquake [*Wesson et al.*, 1971]). (2) It is a barrier [*Das and Aki*, 1977], perhaps formed by a ramp in the fault directly beneath the ridge. (3) The excess overburden associated with the ridge topography generates a strong patch on the fault surface directly beneath it.

The excess overburden in explanation (3) can be roughly estimated by calculating the gravity-induced stresses under long symmetric ridges [*Savage and Swolfs*, 1986]. The shear stress resisting motion on the fault plane $\tau = \mu (\sigma_n - P_f)$ is estimated with and without topography (μ is the coefficient of friction, σ_n is the normal stress, and $P_f = \lambda \sigma_{vertical}$ is the pore fluid pressure for some lithostatic stress $\sigma_{vertical}$ and constant λ). We approximate the Racha ridge as a 2-km-high symmetric ridge and 7 km half-width, with μ = 0.75 and λ = 0.4 (hydrostatic conditions) and a density of 2800 kg/m^3. We assume a fault plane dipping 25° with a base 8.5 km deep under the ridge center. The resulting maximum perturbation to τ due to the topographic load is 17 MPa, at a depth of 5-6 km on the fault plane. Comparison with the seismicity suggests that the maximum perturbation is not coincident with the gap and that the expected perturbations vary gradually along the fault surface with depth. It is unclear how

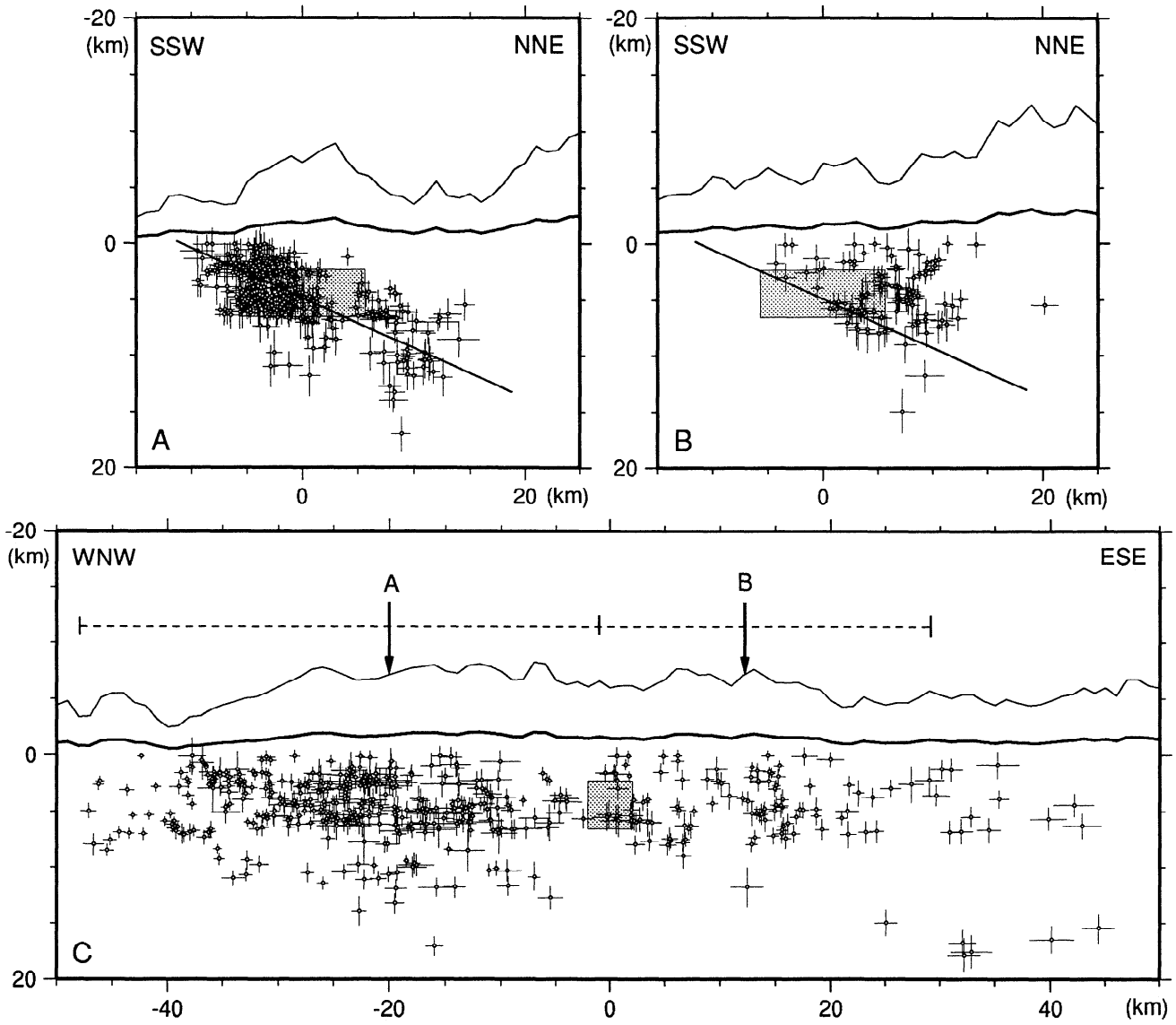

Figure 13. Cross sections of best aftershock locations, as described in text (also see Figures 12 and 15) and the corresponding topography. The bars show the 68% confidence limits for the hypocenter location errors in latitude, longitude, and depth (there is no error larger than ±2 km). Heavy line shows topography with no vertical exaggeration; light line shows 4 × vertical exaggeration. Inclined line shows dip of main shock nodal plane. (a) Western zone projected along the direction N20°E to the right end. (b) Eastern zone, not including aftershocks of June 15 event, projected along the direction N20°E to the right end. (c) All aftershocks (494 events, including aftershocks of June 15 event) projected along strike (E20°S direction to the right end), showing intersection of cross sections A and B. Cross sections A and B are located in Figure 15. The left and right dashed segments show the extent of the western and eastern zones in Figures 13a and 13b, respectively. The origin of coordinates is the epicenter of the mainshock (event I, Table 3). The solid boxes show the mainshock's formal errors in latitude, longitude, and depth (Tables 3 and 4).

such a static stress change can affect the frictional properties along the fault, and little is known about the frictional properties of large-offset thrust faults, but it is interesting to notice that the predicted perturbation to τ (17 MPa) is much larger than the inferred static stress drop (1.4-4.5 MPa, based on the seismic moment and fault area inferred from aftershocks). This suggests it would be of interest to examine the relationship between topography and seismicity on other low-angle fault systems.

Slip and Rate of Shortening

The slip inferred for this earthquake gives some indication of the relation between the causative thrust fault system and the observed topography. The seismic slip D is estimated from the observed seismic moment M_o and the fault plane area $L \times W$ (L is along-strike length, and W is downdip width) inferred from the early aftershock distribution using standard relationships and a shear modulus consistent with the velocity model (3×10^{10} N m^{-2}). An upper bound on aftershock area corresponds to the complete area of pre-June 15 aftershocks $L \times W \cong 75 \times 15$ km^2, and a reasonable minimum is $L \times W \cong 50 \times 10$ km^2. For example, the latter could be the case if the mainshock ruptured only the western part of the aftershock distribution. These bounds give a slip estimate $0.8 < D < 1.8$ m, and a slip-to-fault length ratio of $1.1 \times 10^{-5} < D/L < 3.6 \times 10^{-5}$, similar to interplate values elsewhere [*Scholz et al.*, 1986]. The ratio is lower than that for most plate interior earthquakes, suggesting that the active fault has strength characteristics more similar to plate boundary faults, consistent with significant slip in many previous earthquakes.

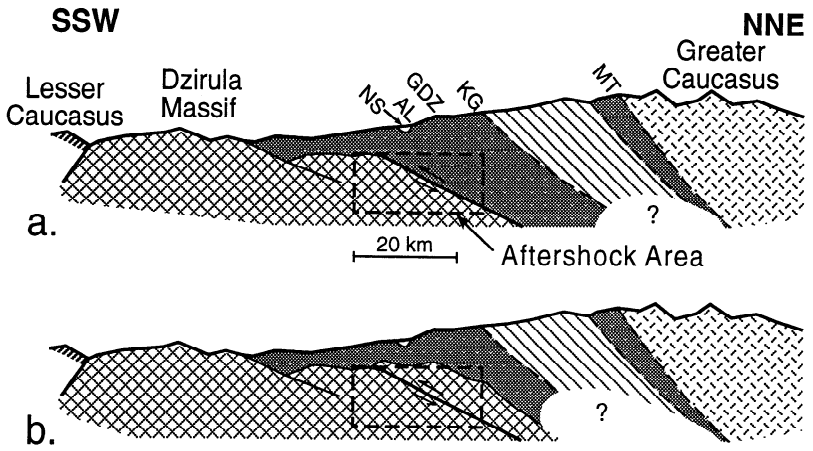

Figure 14. Two possible interpretations of the main fault. (a) Fault thrusts sediment over basement. (b) Fault lies within shallow basement. Abbreviations are AL, Abkhaz-Lechkum fault; GDZ, Gagra-Dzhava zone; KG, Krasnuopolyansk-Guzduchay overthrust; MT, Main overthrust; and NS, Neogene sediments. Rock units are denoted by the same convention as in Figure 12. The topography is sketched with 4 × vertical exaggeration.

Assuming Airy isostasy and mass balance, about 33 km of shortening is required in order to generate the observed topography. The actual convergence may have been much more, because erosion has removed material. The present thrust front system may have been active since middle upper Pliocene (~2.5 Ma) when intensified deformation started at that time [*Burtman*, 1989], although the ~5 m.y. change in clastic sediment sources may instead mark the onset of shortening. Hence average shortening rates of 6-13 mm/yr or more may be required to generate the observed topography. By comparison, geological

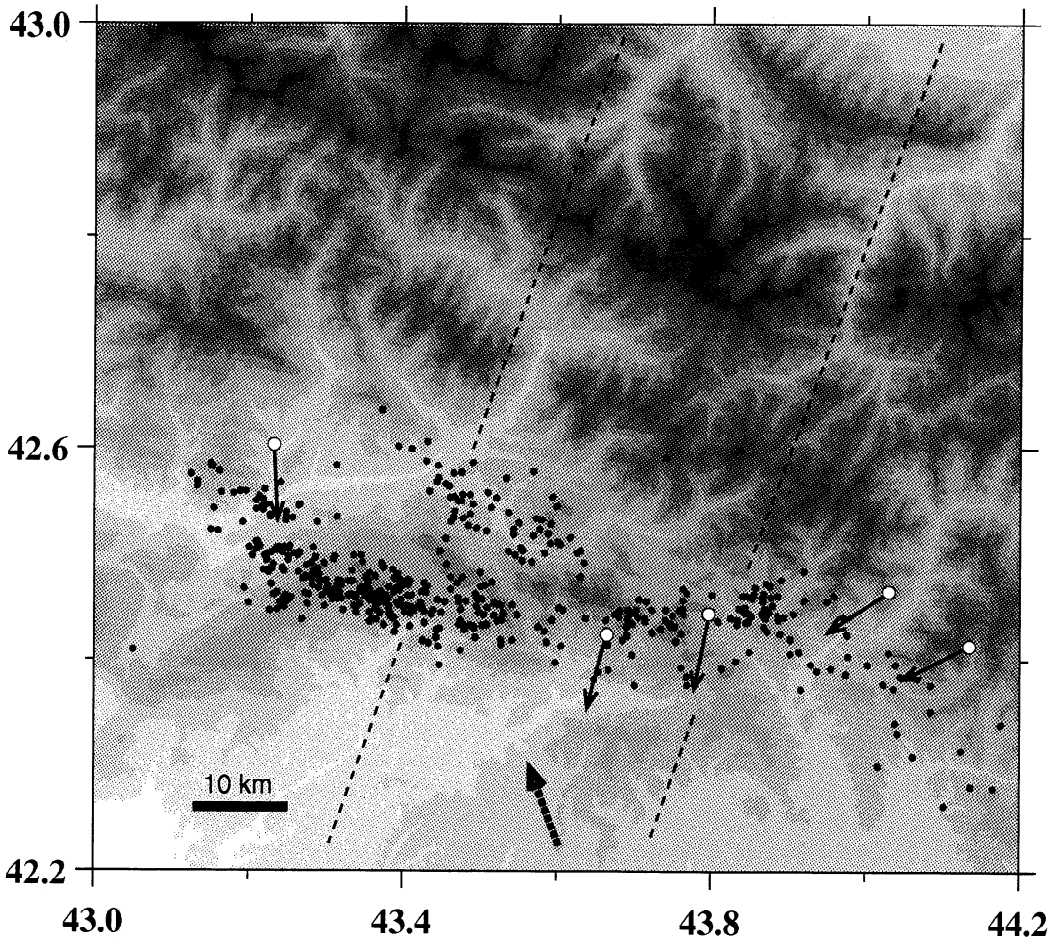

Figure 15. Aftershocks and topography. Best located aftershocks (494 events), as described in text. Topography is contoured at 400-m intervals. Note close correlation of main aftershock zone with ridge on southern flank of mountains. Elevation range is 200 m (white) to 4800 m (black). Open circles are epicenters of the events I, II, III, IV and V (Table 3 and Figures 4d and 12). Light arrows show direction of slip vectors. Large dashed arrow shows relative direction of motion of the Arabian plate with respect to Eurasia [*DeMets et al.*, 1990]. Dotted lines show locations of the cross sections in Figures 13a and 13b.

estimates for individual thrust surfaces in the Greater Caucasus give late Cenozoic shortening values of 5-60 km [*Dotduyev*, 1986; *Gamkrelidze and Gamkrelidze*, 1977]. Adopting a shortening estimate of 10 km for the last 2.5 m.y., convergence would occur across the Greater Caucasus at 4 mm/yr. These estimates show that repeated earthquakes, similar to the Racha earthquake (i.e., every 250 years with a horizontal component of slip of ~1 m), can contribute significantly to mountain building and could form the Greater Caucasus in a reasonable amount of time.

Before the 1991 Racha earthquake, *Westaway* [1990] argued that the western Greater Caucasus is shortening less rapidly than its eastern section. The 1991 Racha earthquake sequence shows that the seismicity levels in western and eastern Caucasus are comparable, and there is no reason to think that shortening rates are different. Similar topography and geological shortening also support equivalent modern rates in the two regions.

Fault Segmentation: Slip Rate Changes or Rheology?

The eastern termination of the aftershock zone coincides with several important structural discontinuities: (1) north of the thrust front, the eastern end of the Gagra-Dzhava zone and the intersection of its bounding faults; (2) the local change of direction and nature of the thrust front; and (3) south of the thrust front, the boundary between the eastern end of the outcrop of the Dzirula massif to the west and the Karthaliny basin to the east. Also, the axis of the Greater Caucasus changes from a W-NW direction to a more W-E direction (Figure 1). As discussed above, a NE trending, left-lateral strike-slip zone had been inferred to separate the east and west Greater Caucasus near 44°E [e.g., *Philip et al.*, 1989; *Westaway*, 1990], supposedly accommodating a significant change in slip rates.

However, the 1991 events and a reevaluation of structures demonstrate that significant shortening may occur in the western Greater Caucasus. We find no direct evidence for an east-west gradient in shortening and no evidence for a strike-slip transfer structure. Rather, we suspect that the along-strike structural discontinuities represent significant changes in the mechanical properties of the collision zone that result in different styles of deformation east and west of 44°E. Changes in deformational style can account for most evidence used to argue for a shear zone in the northern Caucasus. The absence of the exposed Dzirula massif to the east, and possible underthrusting of the Caspian Sea basin under the northern boundary of the Greater Caucasus may contribute significantly to mechanical behavior changes. The Dzirula massif seems to correspond to a northward step of the thrust belt trace, perhaps because its buoyancy or high topography impedes the southward advance of thrust sheets while they are unimpeded in adjacent sedimentary basins.

The aftershock distribution, the focal mechanism of the main shock, and the two larger aftershocks suggest a complicated fault geometry. However, the complexities in the inferred rupture pattern correlate well with complexities in surface structures, in particular with the discontinuities discussed above near 44°E. The correlation of these discontinuities with the aftershock pattern is evidence that along-strike geological and structural discontinuities can control the bounds of rupture of the main shock and its aftershock sequence. The coincidence of these discontinuities with others at a larger regional scale may indicate a long-term geological control on fault segmentation.

Slip Vectors, Surface Structures, and Internal Deformation

The slip vectors of the mainshock and four larger aftershocks have a different orientation from the relative movement vector of the Arabian plate with respect to Eurasia (Figure 15). Some of the divergence is probably caused by a partitioning of the strike-slip motion to the south [Jackson, 1992]. However, local effects such as topography-related buoyancy forces may be equally important. Events III and V (Table 4 and Figures 12 and 15) show slip vectors rotated 41° and 49° clockwise from the mainshock. These directions are perpendicular to the local structural trend rather than parallel to a common transport direction (Figure 16a). One could imagine a somewhat different behavior of these two faults whereby the slip vectors show the same direction of transport (Figure 16b), in which case no internal deformation of the overriding mountains would be required. The slip vectors imply that the thrust front is not moving in a single, coherent direction, so active structures must be present that decrease the along-strike length of the mountain ranges. Such deformation is similar to that inferred from along-strike slip vector rotation in island arcs [*McCaffrey*, 1991] and collision zones [Abers and McCaffrey, 1994]. In the Caucasus, unlike many island arcs, it appears that slip vectors remain perpendicular to the fault plane strike so that slip occurs without any component of oblique or along-strike motion, perhaps because the upper plate is weak and deforms easily [e.g., *Fitch*, 1972; *McCaffrey*, 1991]. It is unclear where the along-strike shortening is occurring, but the ~41° change in slip direction requires that the E-W shortening rate within the thrust sheet is roughly 70% of the N-S shortening rate across the thrust fault.

These observations suggest a strong control of earthquake slip vectors by local structures or by topography rather than by distant plate motions. One consequence of this behavior is that the regional strain cannot be safely determined from the moment

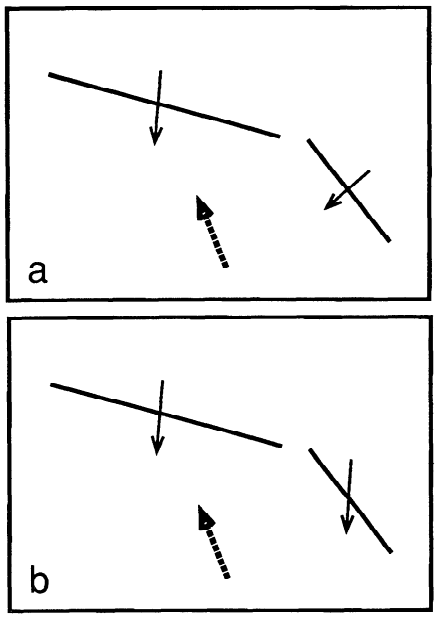

Figure 16. (a) Sketch of two faults resembling the thrust front of the Greater Caucasus activated by the 1991 earthquakes and its corresponding slip vectors. The thrust front is not moving in a single, coherent direction. Internal deformation of the range is required. Large dotted arrow shows relative direction of motion of the Arabian plate respect to Eurasia. (b) Same as Figure 16a but in the case where the slip vectors are parallel. The direction of transport is the same for both fault segments, and no differential deformation along strike would be required. However, the scenario in Figure 16b is not observed.

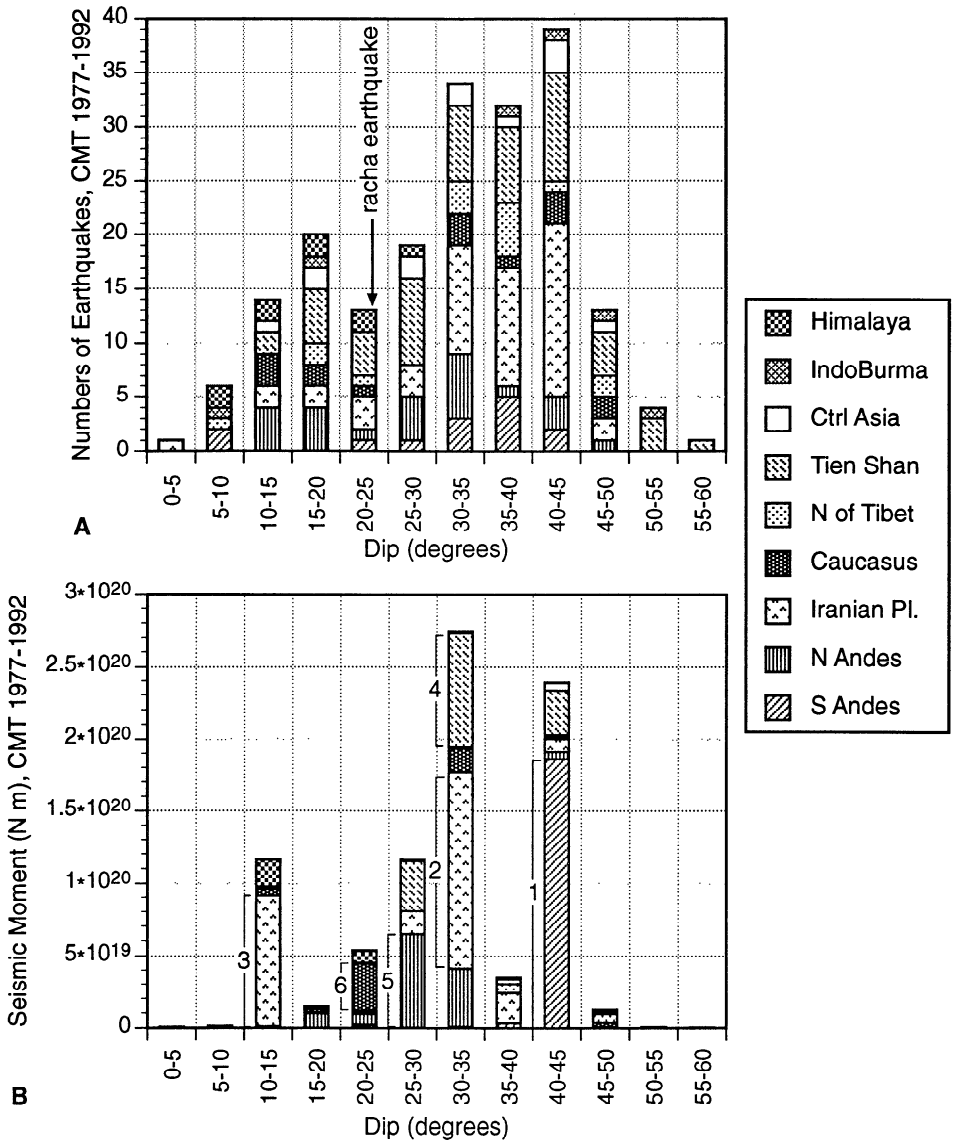

Figure 17. (a) Number of shallow-plane dips on continental intraplate thrust earthquakes in the Harvard centroid moment tensor catalog (CMT) 1977-1992 [e.g., *Dziewonski et al.*, 1992a]. Events are selected from various thrust belts for depth less than or equal to 40 km, P axis plunge P_{PL} < T axis plunge T_{PL}, and $\sqrt{P_{PL}^2 + T_{PL}^2} > 45°$. (b) Sum of the seismic moment release (CMT moment) for the earthquakes in Figure 17a on the same dips intervals. 1, 2, 3, 4, 5, and 6 are the seismic moments of the six largest earthquakes (the dates are mentioned in the text). Moment 6 corresponds to the Racha earthquake. Note that the Racha earthquake is incorporated in both histograms in the 20°-25° dip interval according to the results of this paper, and not with the CMT's dip.

tensors of a small number of earthquakes. This could be true for many tectonically active continental areas formed by a collage of fault-bound fragments, for example throughout much of the wide deformational region between Eurasia and the Arabian plate (Figure 1).

Dip of Continental Thrust Faults

The inferred fault plane of the 1991 mainshock has a moderately low dip (~24°), unlike many other continental thrust earthquakes. This is demonstrated by comparing our results to a compilation from the CMT catalog, 1977-1992, of all shallow earthquakes in continental thrust belts with thrust mechanisms (Figure 17a). The fault plane dips on Figure 17 are plotted assuming that the shallower-dipping nodal plane is always the fault plane. A counterexample is the 1988 Spitak earthquake (Figure 2), for which the fault plane is the steeper nodal plane [*Philip et al.*, 1992; *Westaway*, 1990]. Hence this approach provides a maximum estimate of the numbers of earthquakes with shallow dipping planes. Most events (55%) show dips between 30° and 45°, while 36% have dip less than 30°. The comparison of the dip of the Racha mainshock fault plane to the compilation (Figure 17a) might be considered misleading since the CMT's dip is 39° (Table 4). However, we see no reason to suspect a systematic bias to CMT dips, so the comparison between our well-constrained dip with a statistical distribution of CMT dips should be valid.

The relative maximums of moment release with dip (Figure 17b) coincide to dips where the frequency distribution shows maxima (Figure 17a). However, the largest contributions to the moment sums come from only a few earthquakes. Five large earthquakes ($M_O \geq 0.5 \times 10^{20}$ N m) contribute to the 64% of the total moment release. One in the 40°-45° interval (south Andes,

November 23, 1977), two in 30°-35° (Iranian plateau, September 16, 1978, and Tien Shan, August 19, 1992), one in 25°-30° (north Andes, March 6, 1987), and one in 10°-15° (Iranian plateau, July 28, 1981) contribute to 78%, 76% (48% + 28%), 55%, and 78%, respectively, of the moment release in the corresponding dip intervals. The six largest earthquake is the Racha earthquake (CMT moment). Large earthquakes (as defined above) for dips less than 30° are present only in the 10°-15° and 25°-30° interval (one in Iranian plateau and one in north Andes). The compilation (Figure 17) is restricted to a period of only 17 years, while the recurrence interval for intracontinental earthquakes could be very large. Nevertheless, the rate of occurrence of shallow dipping earthquakes may be insufficient to explain the amount of geologically observed thrust faulting (i.e., shallow-dipping thrust sheets are prevalent in the geological record in most ranges), and in many cases low-angle thrusts may slip aseismically. For example, it seems likely that low-angle detachments in the Hormuz Salt accommodate slip aseismically in the Zagros [e.g., *Jackson and McKenzie*, 1984]. The Racha earthquake example shows that moderate-to-low angle thrust faults can produce earthquakes, but large events along such faults are infrequent.

In the Racha earthquake crystalline rock probably lies on one or both sides of the fault (Figure 14), suggesting that the rheology of the fault zone may be a significant factor controlling the potential of continental thrust sheets for large earthquakes. Many low-angle thrusts, by contrast, abut sedimentary basins. In the M_S = 7.3, 1980 El Asnam earthquake [*Nábělek*, 1985] a shallow thrust (20°) was likely activated as a second subevent in following an event on a deeper fault plane (46°). In the 1991 Racha earthquake sequence a large shallow-dipping thrust (mainshock) and smaller steeper dipping thrusts along the thrust front (aftershocks III, IV and V) are both present. More detailed work is needed to assess the conditions necessary for low-angle continental thrust earthquakes to occur.

Conclusions

The 1991 Racha earthquake represents the thrust faulting that is actively creating the Greater Caucasus. The earthquake and its aftershocks are shallow; the centroid depth is 3-10 km, and most of the aftershocks are between 3 and 12 km. The strike (278°-307°) and dip (20°-31° toward NNE) of the main fault plane determined from body wave inversion are consistent with the aftershocks and surface geology. The ~24° dip is shallower than is often observed in continental thrust earthquakes (30°-45°), making it one of the few seismogenic examples of shallow dipping thrust faults building mountains. With this geometry either (1) the fault decouples low-strength sediments from the more high-strength basement rocks or (2) the basement is directly involved and undergoes shortening.

The primary aftershock area follows the Racha ridge and the eastern end of the Gagra-Dzhava zone. Two western clusters of aftershocks represent either separate activation of faults at two depths or different parts of the same north dipping fault zone separated by an aftershock-free patch. The relationship between the main fault, aftershocks, and the Racha ridge suggest that this ridge may have been formed by repeated earthquakes in the same fault system. Bends, intersections of faults, and lower plate discontinuities appear to control the rupture bounds of the mainshock and aftershock sequence. The discontinuities coincide with many other discontinuities at regional scale, which may indicate a long-term lower plate control on fault segmentation.

The 1991 Racha earthquake shows that the western Greater Caucasus may be actively accommodating convergence at a rate comparable to the eastern Caucasus. Hence a feature like the Borzhomi-Kasbeg zone need not be a major left-lateral shear zone; more likely, it indicates a major along-strike transition in mechanical properties. The differences in mechanical behavior may be controlled by the location of the eastern boundary of the Dzirula accreted block.

The directions of the slip vectors of the mainshock and larger aftershocks are perpendicular to the local trend of the thrust front, despite the change in fault strike, so that the slip vector of event III is rotated ~41° clockwise from the mainshock. This implies that two adjacent segments of the thrust front are converging and that the along-strike length of the mountain range is decreasing. These observations suggest control of the slip vectors by local structures, complicating calculations of the regional strain from the moment tensors of a small number of earthquakes.

Acknowledgments. We are grateful to the field crew (D. Lentrichia of LDEO, and personnel from Kislovodsk and Obninsk); D. Simpson for inspiration and help with catalogs; W. Y. Kim for help with body wave inversion; OME and the Moscow Data center for arrival times; Mark Anders for helpful geological discussions; and Maureen Anders for help with figures. We appreciate the reviews of C. Scholz and L. Sykes. We thank S. Roecker and an anonymous reviewer for comments which substantially improved the manuscript. The data were collected under the auspices of the Joint Seismic Program of IRIS (contract 0174). The analysis was supported by National Science Foundation grant EAR91-18038 and the Air Force Office of Scientific Research grant F 49620-95-1-0026. Lamont-Doherty Earth Observatory contribution No. 5271.

References

Abers, G.A., and R. McCaffrey, Active arc-continent collision: Earthquakes, gravity anomalies, and fault kinematics in the Huon-Finisterre collision zone, Papua New Guinea, *Tectonics*, *13*, 227-245, 1994.

Abers, G.A., and S.W. Roecker, Deep structure of an arc-continent collision: Earthquake relocation and inversion for upper mantle *P* and *S* wave velocities beneath Papua New Guinea, *J. Geophys. Res.*, *96*, 6379-6401, 1991.

Abers, G.A., C. Bryan, S.W. Roecker, and R. McCaffrey, Thrusting of the Hindu Kush over the Tadjik Basin, Afghanistan: Evidence from two large earthquakes, *Tectonics*, *7*, 41-56, 1988.

Abers, G.A., G. Ekström, M.S. Marlow, and E.L. Geist, Bering Sea earthquake of February 21, 1991: Active faulting along the Bering shelf edge, *J. Geophys. Res.*, *98*, 2155-2165, 1993.

Aki, K., and P.G. Richards, *Quantitative Seismology, Theory and Methods*, 557 pp., W.H. Freeman, New York, 1980.

Asanidze, B.Z., D.M. Pechersky, and Sh. A. Adamia, Results of paleomagnetic studies of Paleozoic rocks in the Caucasus (in Russian), *Izv. Acad. Sci. USSR, Phys. Solid Earth*, Engl. Transl., 34-48, 1980.

Bakun, W.H., G.C.P. King, and R.S. Cockerham, Seismic Slip, aseismic slip, and the mechanics of repeating earthquakes on the Calaveras fault, California in *Earthquake Source Mechanics, AGU Geophys. Mono. Ser.* vol. 37, edited by S. Das, J. Boatwright, and C. Scholz, Washington, D.C., 195-207, 1986.

Baranowski, J., J. Armbruster, L. Seeber, and P. Molnar, Focal depths and fault plane solutions of earthquakes and active tectonics of the Himalaya, *J. Geophys. Res.*, *89*, 6918-6928, 1984.

Bazhenov, M.L., and V.S. Burtman, Origin of the Lesser Caucasus structural arc, *Dokl. Akad. Nauk. SSSR*, *293* (2), 416-419, 1987.

Berberian, M., Aftershock tectonics of the 1978 Tabas-e-Golshan(Iran) earthquake sequence: A documented active "thin-and thick-skinned tectonic" case, *Geophys. J. R. Astron. Soc.*, *68*, 499-530, 1982.

Bowman, J.R., G. Gibson, and T. Jones, Aftershocks of the 1988 January 22 Tennant Creek, Australia intraplate earthquakes: evidence for a complex thrust-fault geometry, *Geophys. J. Int.*, *100*, 87-97, 1990.

Burtman, V.S., Kinematics of the Arabian syntaxis, *Geotectonics*, *23*, 139-146, 1989.

Das, S., and K. Aki, Fault plane with barriers: A versatile earthquake model, *J. Geophys. Res.*, *82*, 5658-5670, 1977.

DeMets, C., R.G. Gordon, D.F. Argus, and S. Stein, Current plate motions, *Geophys. J. Int.*, *101*, 425-478, 1990.

Dotduyev, S.I., Nappe structure of the Greater Caucasus Range, *Geotectonics, 20*, 420-430, 1986.

Dziewonski, A.M., and D.L. Anderson, Preliminary reference Earth model, *Phys. Earth Planet. Inter.*, *25*, 297-356, 1981.

Dziewonski, A.M., G. Ekstrom, and M.P. Salganik, Centroid-moment tensor solutions for April-June 1991, *Phys. Earth Planet. Inter.*, *71*, 6-14, 1992a.

Dziewonski, A.M., G. Ekström, and M.P. Salganik, Centroid-moment tensor solutions for July-September 1991, *Phys. Earth Planet. Inter.*, *72*, 1-11, 1992b.

Ekström, G., A broad band for earthquake analysis, Ph.D. thesis, Harvard Univ., Cambridge, Mass., 1987.

Ekström, G., R.S. Stein, J.P. Eaton, and D. Eberhart-Phillips, Seismicity and geometry of a 110-km-long blind thrust fault, 1, The 1985 Kettleman Hills, California, earthquake, *J. Geophys. Res.*, *97*, 4843-4864, 1992.

Fitch, T.J., Plate convergence, transcurrent faults, and internal deformation adjacent to southeast Asia and the western Pacific, *J. Geophys. Res.*, *77*, 4432-4460, 1972.

Gamkrelidze, P.D., Geological structure of the Adzhar-Trialet folded system (in Russian), *Tr. Geol. Inst. Akad. Nauk. Gruz. SSR*, *2*, 508 pp., 1949.

Gamkrelidze, P.D., and I.P. Gamkrelidze, Tectonic nappes of the southern slope of the Greater Caucasus (within Georgia), *Metsniyereba*, Tbilisi, 81 pp., 1977.

Godzikovskaya, A.A., Mantle earthquakes of Caucasus in region of Tersk-Sunzhen' downwarp, *Izv. Earth Phys.*, *24*, 586-590, 1988.

Godzikovskaya, A.A., and G.I. Reysner, *Geotectonics*, *23*, 205-213, 1989.

Gorshkov, G.P., *Regionalnaya Seismotektonika Territorii Yuga SSSR: Alpiiskii Poyas* (in Russian), Nauka, Moscow, 1984.

Harvey, D., and G.L. Choy, Broad band deconvolution of GDSN data, *Geophys. J. R. Astron. Soc.*, *69*, 659-668, 1982.

Jackson, J., Partitioning of strike-slip and convergent motion between Eurasia and Arabia in eastern Turkey and the Caucasus, *J. Geophys. Res.*, *97*, 12471-12479, 1992.

Jackson, J., and D. McKenzie, Active tectonics of the Alpine-Himalayan Belt between western Turkey and Pakistan, *Geophys. J.R. Astron. Soc.*, *77*, 185-264, 1984.

Kennett, B.L.N., and E.R. Engdahl, Travel times for global earthquake location and phase identification, *Geophys. J. Int.*, *105*, 429-465, 1991.

Khain, V.E., *Regional Geotectonics, Outer-Alpine Asia and Australia* (in Russian), 356 pp., Nedra, Moscow, 1979a.

Khain, V.E., The Late Triassic North Caucasian-Turkmen-North Afghan volcanic belt and opening of the North Tethys zone (in Russian), *Dokl. Akad. Nauk. SSSR*, *249*, 1190-1192, 1979b.

Khain, V.E., *Regional Geotectonics, Alpine Mediterranean Belt* (in Russian), 344 pp., Nedra, Moscow, 1984.

Khalilov, E.N., Sh. F. Mekhtiev, and V.E. Khain, Some geophysical data confirming collisional origin of the Great Caucasus (in Russian), *Geotektonika*, *2*, 54-60, 1987.

Klein, F.W., Hypocenter Location Program HYPOINVERSE Part 1: Users Guide to Versions 1, 2, 3, and 4, *U.S. Geol. Surv.*, Open File Rep., *78-694*, 1978.

Kopp, M.L., and I.G. Shcherba, History of late Alpine development of the eastern Caucasus, *Geotektonika*, *6*, 94-108, 1985.

Lebedeva, T.D., Earthquakes in the Caucasus with subcrustal foci, *Tr. Geol. Inst. Akad. Nauk. Gruz. SSR*, *17*, 139-159, 1958.

Lerner-Lam, A., G. Abers, D. Lentrichia, N. Zakharchenko, and V. Mishatkin, Joint US/USSR survey of Georgian/Ossetian earthquake aftershock sequence, *IRIS Newslett.*, *10*(2), 10-11, 1991.

McCaffrey, R., Slip vectors and stretching of Sumatran fore arc, *Geology*, *19*, 881-884, September 1991.

McCormack, D.A., A. Cisternas, S. Arefiev, and C. Langer, The April 29, 1991 Ratcha, Georgia SSR earthquake, *Seismol. Res. Lett.*, *63*, pp. 26, 1992.

McKenzie, D.P., Active tectonics of the Mediterranean region, *Geophys. J.R. Astron. Soc.*, *30*, 109-185, 1972.

Milanovsky, E.E., and V.E. Khain, Geologicheskoe stroenie Kavkaza (in Russian), *Izd. Mos. Gos. Univ. Ocherki Regionalnoi Geol. SSSR*, no. 8, 357 pp., 1963.

Molnar, P., Structure and tectonics of the Himalaya: Constraints and implications of geophysical data, *Annu. Rev. Earth Planet Sci.*, *12*, 489-518, 1984.

Molnar, P. and Chen, W.-P., Seismicity and mountain building, in *Mountain Building Processes, edited by K.J. Hsu*, pp. 41-57, Academic, San Diego, Calif., 1983.

Nábělek, J.L., Determination of earthquake source parameters from inversion of body waves, Ph.D. thesis, 361 pp., Mass. Inst. of Technol., Cambridge, 1984.

Nábělek, J.L., Geometry and mechanism of faulting of the 1980 El Asnam, Algeria, earthquake from inversion of teleseismic body waves and comparison with field observations, *J. Geophys. Res.*, *90*, 12713-12728, 1985.

Nalivkin, D.B. (Ed.), Geological map of Caucasus, scale 1:500,000, Min. of Geol. of the USSR, Moscow, 1976.

Nelson, M.R., R. McCaffrey, and P. Molnar, Source parameters for 11 earthquakes in the Tien Shan, Central Asia, determined by *P* and *SH* waveform inversion, *J. Geophys. Res.*, *92*, 12629-12648, 1987.

Philip, H., A. Cisternas, A. Gvishiani, and A. Gorshkov, The Caucasus: An actual example of the initial stages of continental collision, *Tectonophysics*, *161*, 1-21, 1989.

Philip, H., E. Rogozhin, A. Cisternas, J.C. Bousquet, B. Borisov and A. Karakhanian, The Armenian earthquake of 1988 December 7: Faulting and folding, neotectonics and palaeoseismicity, *Geophys. J. Int.*, *110*, 141-158, 1992.

Richards, P. G., D.C. Witte, and G. Ekström, Generalized ray theory for seismic waves in structures with planar nonparallel interfaces, *Bull. Seismol. Soc. Am.*, *81*, 1309-1331, 1991.

Roecker, S.W., Velocity structure of the Pamir-Hindu Kush region: Possible evidence of subducted crust, *J. Geophys. Res.*, *87*, 355-369, 1982.

Roecker, S.W., Y.H. Yeh and Y.B. Tsai, Three-dimensional *P* and *S* wave velocity structures beneath Taiwan: Deep structure beneath an arc-continent collision, *J. Geophys. Res.*, *92*, 10547-10570, 1987.

Roecker, S.W., J.L. Chatelain, B.L. Isacks, and R. Prevot, Anomalously deep earthquakes beneath the New Hebrides trench, *Bull. Seismol. Soc. Am.*, *78*, 1984-2007, 1988.

Ruppel, C., and M. McNutt, Regional compensation of the Greater Caucasus mountains based on an analysis of Bouguer gravity data, *Earth Planet. Sci. Letters*, *98*, 360-379, 1990.

Satian, M.A., A.A. Belov, and S.A. Adamiya, Seminar-School on "The Geodynamics of the Caucasus," *Geotectonics*, *21*, 1987.

Savage, W.Z., and H.S. Swolfs, Tectonic and gravitational stress in long symmetric ridges and valleys, *J. Geophys. Res.*, *91*, 3677-3685, 1986.

Scholz, C.H., The Mechanics of Earthquakes and Faulting, Cambridge University Press, New York, 1990.

Scholz, C.H., C.A. Avilles, and S.G. Wesnousky, Scaling differences between large interplate and intraplate earthquakes, *Bull. Seismol. Soc. Am.*, *76*, 65-70, 1986.

Stein, R.S., and G. Ekström, Seismicity and geometry of a 110-km-long blind thrust fault, 2, Synthesis of the 1982-1985 California earthquake sequence, *J. Geophys. Res.*, *97*, 4865-4883, 1992.

Stein, S., and D.A. Wiens, Depth determinations for shallow teleseismic earthquakes: Methods and results, *Rev. Geophys.*, *24*, 806-832, 1986.

Suárez, G., P. Molnar, and B.C. Burchfield, Seismicity, fault-plane solutions, depth of faulting, and active tectonics of central Andes, *J. Geophys. Res.*, *88*, 10403-10428, 1983.

Tarantola, A., and B. Valette, Inverse problems=Quest for information, *J. Geophys.*, *50*, 159-170. 1982.

Tskhakaya, A.D., Deep Caucasus earthquakes, *Izv. Akad. Nauk. SSSR*, Ser. geofiz., no. 5, 577-584, 1962.

Wesson, R.L., W.H.K. Lee, and J.F. Gibbs, The San Fernando, California, earthquake of February 9, 1971, *U.S. Geol. Surv. Prof. Pap.*, 24-29, 1971.

Westaway, R., Seismicity and tectonic deformation rate in Soviet Armenia: Implications for local earthquake hazard and evolution of adjacent regions, *Tectonics, 9,* 477-503, 1990.

Wiens, D. A., Bathymetric effects on body waveforms from shallow subduction zone earthquakes and application to seismic processes in the Kurile Trench, *J. Geophys. Res., 94,* 2955-2972, 1989.

Zaharova, A.I., I.P. Gabsatarova, O.E. Starovoit, and L.S. Chepkunas, The main source parameters of the Racha Earthquake and its aftershocks, *Phys. Earth,* no. 3, 1993.

Zhang, J., and T. Lay, A new method for determining the long-period component of the source time function of large earthquakes, *Geophys. Res. Lett., 16,* 275-278, 1989.

Zonenshain, L.P., and X. Le Pichon, Deep basins of the Black Sea and Caspian Sea as remnants of mesozoic back-arc basins, *Tectonophysics, 123,* 181-211, 1986.

Zonenshain, L.P., M.I. Kuzmin, and L.M. Natapov, Alpine-Himalayan Foldbelt Within the USSR, in Geology of the USSR, A Plate-Tectonic Synthesis, Geodyn. Ser., vol. 21, edited by B. M. Page, pp. 167-179, AGU, Washington, D.C., 1990.

G. A. Abers, Department of Geology, Lindley Hall, University of Kansas, Lawrence, KS 66045. (email: abers@kuhub.cc.ukans.edu)

A. L. Lerner-Lam and E. G. Triep, Lamont-Doherty Earth Observatory, P.O. Box 1000, Route 9W, Palisades, NY 10964-8000. (email: triep@lamont.ldgo.columbia.edu)

V. Mishatkin, O. Starovoit, and N. Zakharchenko, OME, Institute of the Physics of the Earth, 189 Lenin St., Obninsk, Kaluga Obl. 249020, Russia. (email: ome@idahub.ucsd.edu)

(Received July 28, 1994; revised September 22, 1994;
accepted September 29, 1994.)